

## REVERBERATION MAPPING OF LUMINOUS QUASARS AT HIGH-Z

PAULINA LIRA<sup>1</sup>, SHAI KASPI<sup>2</sup>, HAGAI NETZER<sup>3</sup>, ISMAEL BOTTI<sup>4</sup>, NIDIA MORRELL<sup>5</sup>, JULIÁN MEJÍA-RESTREPO<sup>1</sup>, PAULA SÁNCHEZ<sup>1</sup>, JORGE MARTÍNEZ<sup>1</sup>, PAULA LÓPEZ<sup>1</sup>

(Received; Revised; Accepted)  
*Draft version July 30, 2018*

### ABSTRACT

We present Reverberation Mapping (RM) results for 17 high-redshift, high-luminosity quasars with good quality R-band and emission line light curves. We are able to measure statistically significant lags for Ly $\alpha$  (11 objects), SiIV (5 objects), CIV (11 objects), and CIII] (2 objects). Using our results and previous lag determinations taken from the literature, we present an updated CIV radius–luminosity relation and provide for the first time radius–luminosity relations for Ly $\alpha$ , SiIV and CIII]. While in all cases the slope of the correlations are statistically significant, the zero points are poorly constrained because of the lack of data at the low luminosity end. We find that the emissivity weighted distance from the central source of the Ly $\alpha$ , SiIV and CIII] line emitting regions are all similar, which corresponds to about half that of the H $\beta$  region. We also find that 3/17 of our sources show an unexpected behavior in some emission lines, two in the Ly $\alpha$  light curve and one in the SiIV light curve, in that they do not seem to follow the variability of the UV continuum. Finally, we compute RM black hole masses for those quasars with highly significant lag measurements and compare them with CIV single–epoch (SE) mass determinations. We find that the RM-based black hole mass determinations seem smaller than those found using SE calibrations.

*Subject headings:* galaxies: active — surveys — variability

### 1. INTRODUCTION

These days it is widely accepted that all massive galaxies harbor a massive Black Hole (BH) in their centers (Kormendy & Ho, 2013). To determine the properties of these BHs is therefore crucial for the understanding of galaxy formation and evolution. The ability to measure BH masses and accretion rates in AGN using reverberation mapping techniques has enabled real physical comparison between active and dormant BHs in the local universe, but BH mass estimates from AGN become even more crucial at high- $z$  since stellar dynamical estimates from the study of normal galaxies are clearly not feasible at redshifts of cosmological interest ( $z > 1$ ).

Reverberation Mapping (RM) uses the lag between variations in the central ionizing source and the response of the Broad Line Region (BLR) emission lines to directly measure the BLR size (Blandford & McKee, 1982). Assuming a gravitationally bound system and measuring the BLR line widths, it is possible to infer the mass of the central BH. This assumption has proven to be correct for those objects with measurements from several lines: the observed anti-correlation between the line Doppler widths and their distance from the central black hole, are consistent with virialized motion of the BLR gas in the deep potential of the central BH (Onken & Peterson 2002).

To date reverberation mapping results cover almost 5 orders of magnitude in luminosity but are still limited to luminosities  $\lambda L_{\lambda}(5100\text{\AA}) < 10^{46}$  erg/sec, with the bulk of sources found well below  $< 10^{45}$  erg/sec (e.g., Kaspi et al. 2000, 2005, 2007, Peterson et al. 2004, Bentz et al. 2006, 2009, 2013). Hence, such results cannot be directly applied to high- $z$ , high- $L$  sources, that contain the most massive BHs, since measuring their BLR size requires an extrapolation by up to *two orders of magnitude* in luminosity. This hampers the calibration of the so called radius–luminosity relations, which enable the determination of BH masses from a single spectroscopic observation without requiring source monitoring. ‘Single–epoch’ black hole mass determinations are readily obtained from large spectroscopic surveys, but require the extrapolation of the radius–luminosity relation when high- $z$ , high-luminosity quasars are studied. It is therefore clear that to have statistically significant results for BH demographics and their mass growth with cosmic time, it is first necessary to determine well calibrated radius–luminosity relations that are representative of the full span of AGN luminosity.

So far the few attempts to carry out reverberation mapping of very high-luminosity quasars have seldom proved successful (e.g., Welsh et al. 2000, Trevese et al. 2006, Kaspi et al. 2007, Trevese et al. 2014, Saturni et al. 2016). There are mainly two reasons for this: first, most high-luminosity sources show very low amplitude variations ( $< 20\%$ ) on short time scales and require very extended (many years) monitoring to observe significant flux variations and to overcome the  $(1+z)$  time delay. Second, as it is usually observed in monitoring campaigns, amplitudes for emission line light curves are smaller than that of the continuum emission, as the emission line response is averaged over the very large ( $\sim 1$  pc) quasar BLR geometry. As monitoring of high-

<sup>1</sup> Departamento de Astronomía, Universidad de Chile, Casilla 36D, Santiago, Chile.

<sup>2</sup> Wise Observatory, School of Physics and Astronomy, Tel Aviv University, Tel Aviv 69978, Israel

<sup>3</sup> School of Physics and Astronomy, Tel Aviv University, Tel Aviv 69978, Israel

<sup>4</sup> Facultad de Ingeniería, Universidad del Desarrollo, Av. Plaza 680, Las Condes, Santiago, Chile

<sup>5</sup> Las Campanas Observatory, Carnegie Observatories, Casilla 601, La Serena, Chile

TABLE 1  
SAMPLE SUMMARY

Quasar	$z$	RA DEC (J2000)	R (mag)	$\lambda L_\lambda(1350\text{\AA})$ ( $10^{46}$ ergs $s^{-1}$ )	$\lambda L_\lambda(5100\text{\AA})$ ( $10^{46}$ ergs $s^{-1}$ )	$P_{843}$ MHz (mJy)	$P_{1.4}$ GHz (mJy)	$R_{radio}$	$M_{BH}^{SE}$ (CIV) ( $10^9 M_\odot$ )
CT1061	3.373	10 48 56 -16 37 09	16.20 $\pm$ 0.12	33.88 $\pm$ 3.15	10.28 $\pm$ 0.12	N/A	< 0.5	< 1	3.42
CT250	2.407	04 11 45 -42 54 44	17.69 $\pm$ 0.14	4.97 $\pm$ 0.99	2.88 $\pm$ 0.07	< 6	N/A	< 21	4.65
CT252	1.890	04 18 10 -45 32 17	16.40 $\pm$ 0.10	0.00 $\pm$ 0.00	3.03 $\pm$ 0.06	< 6	N/A	< 6	1.26
CT286	2.556	10 17 23 -20 46 58	16.89 $\pm$ 0.13	11.16 $\pm$ 1.83	6.28 $\pm$ 0.13	N/A	17.7 $\pm$ 0.7	48 $\pm$ 10	2.27
CT320	2.956	13 17 44 -31 47 13	17.82 $\pm$ 0.11	6.35 $\pm$ 0.91	3.86 $\pm$ 0.07	< 6	< 0.5	< 2	6.23
CT367	2.601	22 00 36 -35 02 17	17.14 $\pm$ 0.14	5.89 $\pm$ 1.80	4.66 $\pm$ 0.18	< 6	< 0.5	< 1	5.01
CT406	3.183	10 39 09 -23 13 25	17.66 $\pm$ 0.13	8.13 $\pm$ 0.75	6.18 $\pm$ 0.07	N/A	3.0 $\pm$ 0.5	8.4 $\pm$ 3.4	4.80
CT564	2.659	21 50 15 -44 11 23	17.05 $\pm$ 0.12	9.95 $\pm$ 1.51	3.65 $\pm$ 0.07	< 6	N/A	< 10	1.99
CT650	2.662	04 55 22 -42 16 17	17.28 $\pm$ 0.11	7.59 $\pm$ 1.83	4.77 $\pm$ 0.14	< 6	N/A	< 16	1.88
CT803	2.741	00 04 48 -41 57 28	17.02 $\pm$ 0.12	10.11 $\pm$ 1.20	8.20 $\pm$ 0.12	< 6	N/A	< 5	4.09
CT953	2.535	21 59 54 -40 05 50	17.00 $\pm$ 0.11	9.99 $\pm$ 1.97	6.12 $\pm$ 0.15	< 6	N/A	< 7	5.98
CT975	2.866	22 38 13 -32 48 24	17.46 $\pm$ 0.17	8.78 $\pm$ 1.57	4.70 $\pm$ 0.11	< 6	< 0.5	< 3	5.35
HB890329-385	2.433	03 31 06 -38 24 05	17.54 $\pm$ 0.12	5.80 $\pm$ 0.93	5.40 $\pm$ 0.11	24.3 $\pm$ 1.3	29.8 $\pm$ 1.0	50 $\pm$ 9	6.74
2QZJ002830	2.403	00 28 30 -28 17 06	17.05 $\pm$ 0.14	8.98 $\pm$ 1.74	3.76 $\pm$ 0.09	N/A	< 0.5	< 1	7.64
2QZJ214355	2.620	21 43 55 -29 51 59	17.17 $\pm$ 0.11	9.17 $\pm$ 1.02	2.82 $\pm$ 0.04	N/A	< 0.5	< 2	5.63
2QZJ221516	2.706	22 15 16 -29 44 23	16.71 $\pm$ 0.14	14.29 $\pm$ 1.86	10.18 $\pm$ 0.17	N/A	467 $\pm$ 14	576 $\pm$ 100	1.56
2QZJ224743	2.590	22 47 43 -31 03 07	16.65 $\pm$ 0.10	13.00 $\pm$ 1.05	4.29 $\pm$ 0.04	< 6	2.7 $\pm$ 0.6	5.9 $\pm$ 2.8	15.55

Radio fluxes at 843 MHz and 1.4 GHz were taken from the SUMSS and NVSS catalogs, respectively.

N/A implies that the sources were not covered by the footprint of the survey.

$R_{radio}$  was obtained using the  $P_{1.4}$  GHz measurements, except for unavailable objects ('N/A'), where  $P_{843}$  MHz was used instead.

$\lambda L_\lambda(1350\text{\AA})$  measurements were obtained from the spectroscopic data.

$\lambda L_\lambda(5100\text{\AA})$  luminosities were obtained either from 2MASS photometry or by extrapolating our own R-band magnitudes (see text).

Uncertainties in  $\lambda L_\lambda(1350\text{\AA})$  and  $\lambda L_\lambda(5100\text{\AA})$  were assumed to correspond to the observed R-band variability.

Single-epoch (SE) BH masses ( $M_{BH}^{SE}$ ) have been obtained using the measured CIV FWHM (Mejía-Restrepo et al. 2016).

$z$ , high-luminosity quasars often only samples a few, low amplitude continuum flux variation 'events', the line response can become extremely weak. This requires the ability to measure emission line fluxes to an accuracy of about a few percent (e.g., Kaspi et al., 2007), and the implementation of tailored observing strategies.

In this article we present results from a  $\gtrsim 10$  year monitoring of high- $z$ , high-luminosity quasars. In section 2 we describe the sample selection and data acquisition and treatment. Section 3 deals with time series analysis, while section 4 presents the specifics on the cross-correlation analysis. Section 5 presents the results for the radius-luminosity relations. Finally, section 6 and 7 discusses and summarizes the findings. A concordance cosmology with  $\Omega_m = 0.3$  and  $\Omega_\Lambda = 0.7$  is adopted throughout this paper.

## 2. SAMPLE AND DATA

### 2.1. Sample selection

The targets were drawn from the Calán-Tololo survey (Maza et al., 1996 and references therein), the 2dF QSO Redshift Survey (Croom et al., 2004), and the Hewitt-Burbidge QSO compilation (Hewitt & Burbidge, 1989). They correspond to quasars of very high luminosity, typically  $M_B \sim -29$  magnitudes, located at the high luminosity end of the quasar luminosity function (Bongiorno et al., 2007; Ross et al., 2013). A first spectroscopic run carried out in March 2006 with the du Pont telescope at Las Campanas Observatory (LCO) allowed us to corroborate their quasar nature and the presence of intense emission lines suitable for reverberation mapping. At this redshift range, four lines are readily seen in the spectra of all our quasars: Ly $\alpha$ , SiIV, CIV and CIII].

Towards the end of the monitoring campaign, when confirming the redshift of CT252, we realized that the published value for this source (see Maza et al. (1993),

where a redshift of 2.5 was provided) is much lower than the rest of the sample, at  $z = 1.818$ . This was probably because its very strong and non-symmetric CIV line was mistakingly identified as Ly $\alpha$ . Hence for this source Ly $\alpha$  is not visible in our spectra, but instead we can observe the MgII emission line.

The redshifts for the quasars were obtained from our own data from the CIII] line, except for CT320 where the line fit quality was poor. For this object the CIV redshift is reported instead. For CT252 the MgII redshift is given. Redshifts are found in Table 1 together with some basic information for each quasar such as the R-band magnitude, its standard deviation (see Section 3) and radio flux measurements (see below). Single-epoch virial masses are also reported using the calibration for the CIV emission line presented in Mejía-Restrepo et al. (2016). These were determined using our FWHM measurements of the CIV emission line. A virial factor  $f$  of one was assumed, which is appropriate for velocities estimated from FWHMs (e.g., Grier et al. 2017).

#### 2.1.1. Spectral properties

The mean spectra of each quasar can be seen in Figure 1. These have been flux calibrated and corrected for Galactic extinction assuming the extinction law of Cardelli, Clayton & Mathis (1989) and  $R_V = 3.1$  in the observed frame.  $E(B - V)$  values were in the range of 0.01 to 0.04 magnitudes. For display purposes the spectra have been shifted in the vertical direction ordered by redshift (see caption for details). The absorption feature seen at the constant wavelength of  $\sim 7600\text{\AA}$  corresponds to a telluric O $_2$  absorption. Rest-frame line luminosities, widths and equivalent widths (EWs) are reported in Table 2.

Figure 1 shows rather broad range of spectral properties, from objects with very broad lines, such as CT953

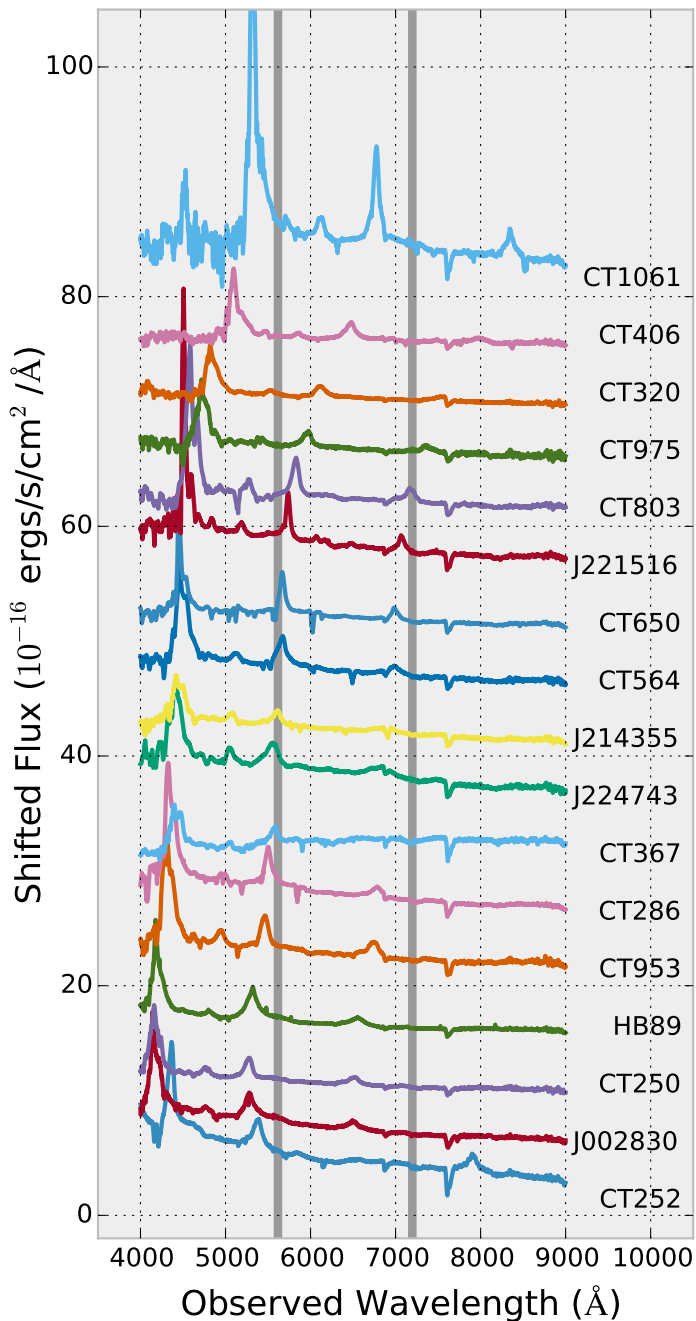


FIG. 1.— Flux calibrated, Galactic extinction corrected, mean spectra of the 17 quasars reported in this work. The spectra have been shifted in the y-axis for display purposes, starting with a zero shift for CT252, 5 units of flux for J002830, 10 units of flux for CT250, and so on. The gray lines approximately demarcate the wavelength region corresponding to the R-band filter.

and J224743, and others with much narrower features, such as CT650 and J221516. Also, the lines can be very prominent (i.e., with large EW), like in the case of CT1061 and CT803, or rather weak (i.e., small EW), such as those in J002839 and J214355. The spectral shapes are rather uniform, with the exception of CT252, for which we are observing a very different spectral range in the rest frame, and CT367, which clearly shows a red spectral shape.

In between gray lines we highlight the 5620-7200 Å wavelength range, which roughly corresponds to the width of the R-band filter. Depending on the redshift of the source, the observed R-band 5620-7200 Å wavelength range corresponds to a mean rest-frame wavelength of 1465 Å for our highest redshift source (CT1061), 1530 Å for our second highest (CT406), and 2271 Å for the lowest redshift source (CT252). The remaining sources are found in the range 1620-1880 Å. It can be seen that this region of the spectra contains the CIII] emission line, which as we will see, does not show strong variability. However, for CT1061, CT320, CT406, CT564, CT650, CT803, CT975 and J221516 the CIV line is redshifted into the R-band coverage. This could affect the analysis of the variability. However, the very broad nature of the R-band and the small amplitude observed in the line variations secures a negligible interference: using the EW values presented in Table 2 and assuming a width of the R-band filter of 2200 Å, it can be seen that the total CIV line flux would contribute at most 10% to the observed-frame R-band photometry.

#### 2.1.2. Radio-loudness and SEDs

It is of interest to determine the radio-loudness of the quasars in our sample. Usually, a radio-to-optical flux-ratio threshold of  $R_{radio} = f(6\text{cm})/f(4400\text{Å}) = 10$  is adopted to separate radio-loud (RL) from radio-quiet (RQ) systems, while values between 10 and 100 are sometimes referred to as radio-intermediate. We searched two surveys for radio sources consistent with the positions of our quasars. First, the Sydney University Molonglo Sky Survey (SUMSS) Source Catalog (Mauch et al. 2003), which covers the southern sky for declinations  $-50 < \delta < -30$  degrees at 843 MHz, reaches a depth of 6 mJy/beam, and has a spatial resolution of  $45 \times 45 / \cos(|\delta|)$  square arcseconds. We also searched the National Radio Astronomy Observatory Very Large Array Sky Survey (NVSS) catalog (Condon et al. 1998), which covers the sky north of -40 degrees at 1.4 GHz, reaching a depth of 0.45 mJy/beam, and with a spatial resolution of 45 arcseconds. The presence of counterparts was confirmed by eye inspection of the radio maps. We K-corrected the radio measurements assuming a power law spectral energy distribution of the form  $S_\nu \propto \nu^{-\alpha}$ , with index  $\alpha = 0.75$  (Wang et al. 2007; Momjian et al. 2014).

To determine the rest-frame optical fluxes we obtained J,H and K magnitudes from the 2MASS All-Sky Catalog of Point Sources (Cutri et al. 2003). No 2MASS photometry was available for CT250, CT286 or CT975. We also obtained fluxes at 5100 Å applying the correlation between continuum emission at 1350 Å and 5100 Å found in Mejía-Restrepo et al. (2016), and extrapolating from our R-band photometry using the quasar rest-frame UV

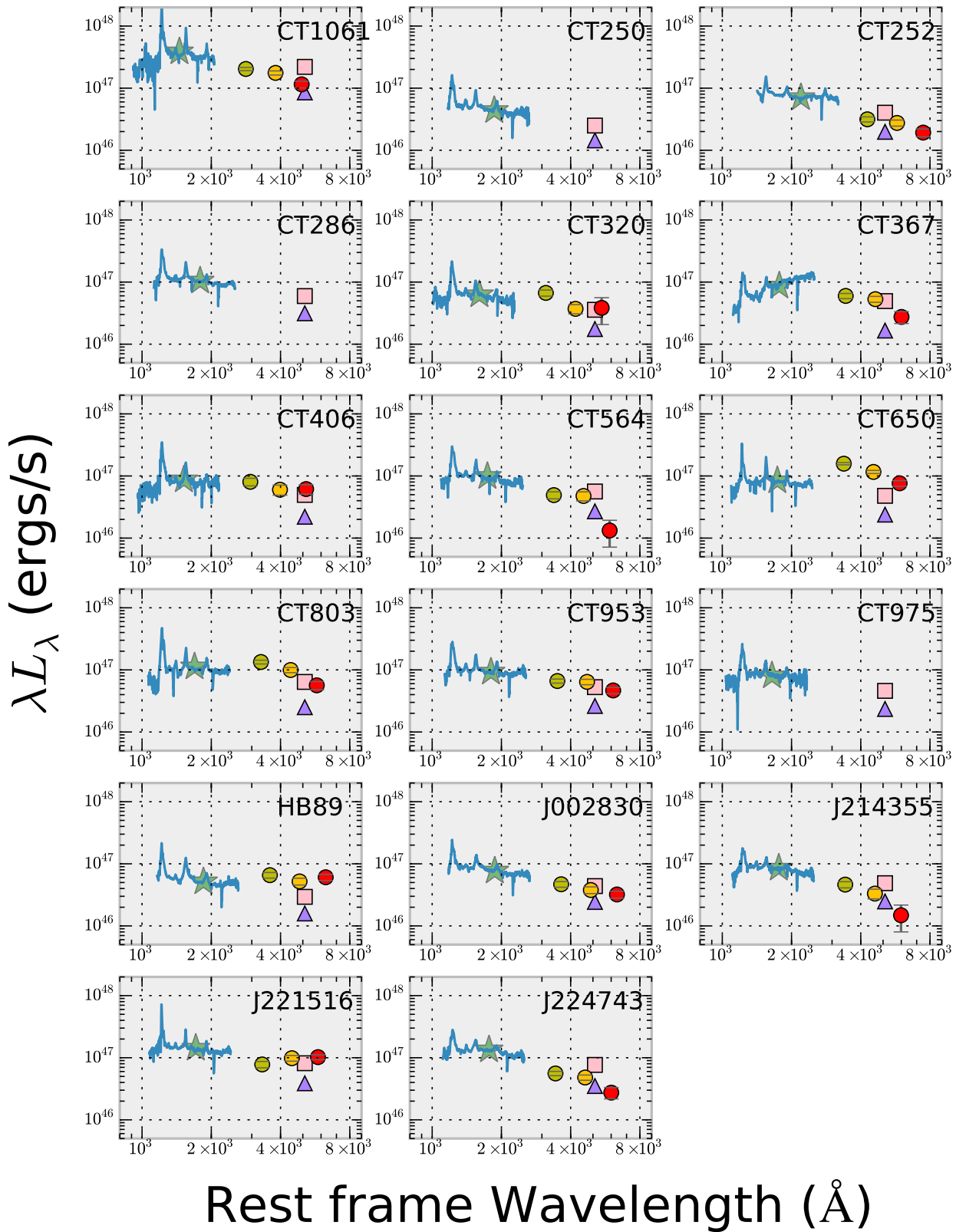


FIG. 2.— Rest-frame Spectral Energy Distributions (SEDs) of the quasars in our sample. Mean spectra for each source are shown together with our  $R$ -band (stars) and JHK 2MASS (circles) photometry. Two extrapolations to  $5100\text{\AA}$  are also included: from  $1350\text{\AA}$  (triangles) using the correlation determined in Mejía-Restrepo et al. (2016), and from the  $R$ -band photometry (squares) using the UV power-law index determined by Vanden Berk et al. (2001).

power-law index ( $\alpha = 0.44$ ) obtained by Vanden Berk et al. (2001).

The Spectral Energy Distributions for our sample are presented in Figure 2. It can be seen that in several cases there is good agreement between the spectra, their extrapolations to  $5100\text{\AA}$  and the 2MASS photometry. However, it is also seen that the extrapolation based on the work by Vanden Berk et al. (2001) is a factor  $\sim 2$  higher than that obtained applying the correlation found in Mejía-Restrepo et al. (2016), which in most cases falls below the 2MASS observations. The relation found in Trakhtenbrot & Netzer (2012) predicts fluxes about half way between the two previous extrapolations. An anomalous case is CT650 (and perhaps CT803 and HB89) which was clearly brighter at the time of the 2MASS observations. CT367 has a spectral shape that is clearly poorly represented by the extrapolation to  $5100\text{\AA}$ , while for J221516 the 2MASS photometry suggests an up-turn of the 2MASS fluxes towards longer wavelengths. In summary, only for those objects without 2MASS photometry and CT650 we will use the spectral  $5100\text{\AA}$  extrapolation based on Vanden Berk et al. (2001) to estimate the rest-frame optical flux. For all other objects, the 2MASS photometry will be adopted. The  $5100\text{\AA}$  luminosities are reported in Table 1. To K-correct the observations to the rest frame  $4400\text{\AA}$  needed to determine  $R_{radio}$ , Vanden Berk et al. (2001) spectral index was again used.

The results on the radio-loudness are reported in Table 1. Three sources were found to be radio-loud quasars: CT286, HB89 and J221516 ( $R_{radio} = 48 \pm 10$ ,  $50 \pm 9$ , and  $576 \pm 100$ , respectively), the last two already noticed as radio-loud systems in the literature (Shemmer et al. 2004; Chhetri et al. 2013). The remaining objects are split into 12 secure radio-quiet systems and two with upper limits above  $R_{radio} = 10$  (CT250 and CT650). Leaving these two last sources aside, a fraction of 3/15 radio-loud quasars is found, which is in good agreement with the general quasar population at the high-end of the luminosity range (Cirasuolo et al., 2003).

## 2.2. Broad-band imaging

Photometric monitoring of  $\sim 50$  high- $z$  AGN started in February 2005. After a few years the less variable systems were dropped and we continue to monitor  $\sim 60\%$  of the original sample. The data were obtained with the 1.3m and 0.9m SMARTS telescopes using broad-band R imaging. Several observations per year were acquired in queue mode. The light curves reported in this work extend until January 2017.

Bias subtraction and flat correction was done in the usual way using IRAF tasks. PSF differential photometry of the quasars was obtained using typically 10-12 local stars. The stars were in turn calibrated against their R-band USNO magnitudes so that the light curves are finally expressed in flux units. Formal photometric errors for the stars were generally small. Therefore a 0.015 magnitude error, as obtained from the median standard deviation of the observed stellar fluxes, was adopted as a more representative photometric error.

## 2.3. Spectroscopy

To secure an accurate relative spectrophotometric calibration we followed Maoz et al. (1990) and Kaspi et al. (2000) and rotated the spectrograph so that the quasar and a comparison star are observed through the same slit. The WFCCD at the du Pont telescope at LCO proved to be a very reliable instrument allowing to position the quasar and comparison star within the slit with sub-pixel precision, for a pixel size of 0.484 arcseconds. The slit width was 8.1 arcseconds wide throughout the observations.

The spectroscopic monitoring started in April 2007 and the latest data were obtained in January 2017. We aimed at having at least one observation per year for each quasar, although weather and instrumental problems sometimes did not allow us to fulfill this goal. Typically each observation consisted of three repeated spectra of 900 to 1200 seconds of exposure time. The spectra were reduced in the standard way using IRAF tasks: bias subtraction and flat calibration were applied using bias frames and internal lamps observed each night. Flats were obtained using the same wide slit as the science frames. One dimensional spectra of the quasar and comparison star were extracted using the same fixed aperture along the spectral direction. Wavelength calibration was determined using helium, neon, argon calibration ‘arcs’ obtained using a narrow slit.

To achieve the relative spectrophotometry, the spectrum of each quasar was divided by the heavily smoothed spectrum of the simultaneously observed comparison star and then the separate ‘normalized-quasar spectra’ were combined. To secure a homogeneous wavelength calibration around the Ly $\alpha$ , SiIV, CIV and CIII] emission lines (and MgII in the case of CT252), sections of the spectra around each line were used to perform a cross-correlation analysis. The spectra were then shifted according to the cross-correlation results. This was particularly important at the blue end of the spectra, where only a few lines from the comparison arcs were available, thus making the wavelength solution rather unreliable.

Line flux measurements were obtained by adopting two small pseudo-continuum windows located at each side of the corresponding emission line. The continuum level under the line in consideration was then assumed to correspond to the interpolation of a straight line joining the mean flux obtained from the pseudo-continuum windows. We checked that the pseudo-continuum windows corresponded to regions with small values in the rms spectrum of each quasar to avoid the presence of weak emission or absorption lines. Likewise, to avoid introducing a spurious line variability signal due to variations of strong self-absorbing features, we limited the line flux measurements to regions devoided of absorption lines, which were readily seen in the rms spectra. As an example, Figure 3 shows the mean and rms spectra for the emission lines in the quasar CT650. The placement of the continuum windows and the region adopted for the line flux measurements are shown. As can be seen, SiIV is heavily absorbed throughout the profile, while the remaining lines show strong and variable absorption in their blue wings. Hence the line fluxes were determined to the right of Ly $\alpha$ , CIV and CIII], while the light curve of the SiIV was obtained from a small spectral window. Notice, however, that if non-variable absorption profiles are present in the line profiles, we do not make any attempt to isolate them

TABLE 2  
LINE MEASUREMENTS

Quasar	Ly $\alpha$			SiIV			CIV			CIII]		
	L ergs s $^{-1}$	EW $\text{\AA}$	FWHM km s $^{-1}$	L ergs s $^{-1}$	EW $\text{\AA}$	FWHM km s $^{-1}$	L ergs s $^{-1}$	EW $\text{\AA}$	FWHM km s $^{-1}$	L ergs s $^{-1}$	EW $\text{\AA}$	FWHM km s $^{-1}$
CT1061	2.1e+46	64	3355	2.4e+45	10	4843	8.9e+45	44	3218	1.4e+45	9	2452
CT250	2.1e+46	64	3355	2.4e+45	10	4843	8.9e+45	44	3218	1.4e+45	9	2452
CT286	2.5e+45	57	6817	3.3e+44	10	6676	1.0e+45	35	6256	3.6e+44	17	5900
CT320	1.3e+45	13	2934	2.8e+44	4	5312	7.8e+44	11	3493	2.3e+44	5	3796
CT367	2.0e+45	33	5368	3.9e+44	9	6453	1.2e+45	33	6844	1.4e+44	5	2085
CT406	1.2e+45	23	4869	1.9e+44	5	3922	1.7e+45	40	6236	2.1e+44	4	8828
CT564	3.8e+45	46	4943	3.8e+44	7	4814	1.8e+45	35	5623	5.9e+44	17	6361
CT650	4.1e+45	52	7007	4.3e+44	6	6053	6.1e+44	10	3419	4.9e+44	12	8593
CT803	1.4e+45	20	2266	1.4e+44	3	3029	1.1e+45	21	3437	6.7e+44	18	4009
CT953	7.3e+45	107	5506	8.0e+44	13	5044	3.1e+45	54	5005	3.4e+44	7	7929
CT975	4.2e+45	47	8199	6.6e+44	10	5875	2.3e+45	40	5970	3.1e+44	7	4468
HB89 0329-385	9.5e+44	14	6275	2.9e+44	5	5231	1.1e+45	22	5831	6.6e+44	19	4070
2QZJ002830	2.4e+45	46	3975	1.7e+44	4	5603	1.9e+45	57	7326	6.7e+44	28	8336
2QZJ214355	1.6e+45	19	4397	2.8e+44	5	6342	7.9e+44	15	6895	3.5e+44	9	4360
2QZJ221516	1.1e+45	15	5857	3.4e+44	6	5239	9.4e+44	17	5888	1.4e+44	4	2893
2QZJ224743	5.0e+45	41	2410	4.8e+44	5	4419	2.2e+45	25	2728	6.5e+44	10	2966
	1.0e+45	10	5206	5.1e+44	6	4685	1.9e+45	23	8861	1.1e+44	2	2010
Quasar	CIV			CIII]			MgII					
	L ergs s $^{-1}$	EW $\text{\AA}$	FWHM km s $^{-1}$	L ergs s $^{-1}$	EW $\text{\AA}$	FWHM km s $^{-1}$	L ergs s $^{-1}$	EW $\text{\AA}$	FWHM km s $^{-1}$			
CT252	1.4e+45	28	5198	2.7e+44	7	4970	4.9e+44	16	3800			

Measurements were obtained from the mean spectrum of each source in the rest frame.

from the line flux measurements.

Errors in emission line measurements were estimated assuming that the line flux  $L$  can be expressed as  $L = \alpha(F - C)$ , where  $\alpha$  is the scaling by the division of the comparison star,  $F$  is the total flux measured in the regions defined for line flux measurement (i.e., between the yellow vertical lines shown in Figure 3) and  $C$  is the interpolated continuum as defined above. Hence, the variance for each line measurement can be written as  $\sigma_\alpha^2(F - C)^2 + \alpha^2(\sigma_F^2 + \sigma_C^2)$ , where  $\sigma$  denotes uncertainty in the quantity given by the subscript.

To estimate  $\sigma_\alpha$ , which encompasses effects such as poor centering of the quasar-star pair on the slit or guiding problems, we determined the ratio of two normalized-quasar spectra obtained during a single observing run. Since typically three observations were obtained per night, two such ratios could be constructed per quasar observation. The ratio distribution using all available data for all quasars can be seen in Figure 4, where the mean and standard deviation of the distribution are also given.

To estimate  $\sigma_F$  we used the error spectrum of each quasar observation (which is obtained assuming photon Poisson statistics and the specific gain and read-out noise of the detector) and determined the total variance as the quadratic sum of the errors from each pixel within the line window. During this step we did not take into account the division by the comparison star as their spectra were heavily smoothed before the division and therefore introduced no further noise.

Finally, to estimate  $\sigma_C$  we resorted to Monte Carlo (MC) simulations because of the rather complex uncertainties that the determination of the continuum level might introduce. For example, continuum window placement can be affected by small mismatches in the wavelength solution, which, in turn, will impact the flux measurement in regions with strong flux fluctuations, like

towards the blue end of the spectra. This is particularly true for the Ly $\alpha$  pseudo-continuum windows, since the normalized quasar continuum flux can increase sharply because of the division by a comparison star with a spectral energy distribution that falls quickly towards the blue. The Ly $\alpha$  blue pseudo-continuum window is also affected by the shape of the continuum due to intergalactic absorption.

We obtained 10000 MC realizations for each line measurement where the flux level in each pseudo-continuum window was determined using fluxes drawn from a Gaussian distribution around the observed window flux values. For the standard deviation of the distribution we adopted the largest value between the flux rms within the pseudo-continuum window and the photon noise derived from the error spectrum within the same window. As expected, for Ly $\alpha$  the flux rms was consistently larger than the photon noise. The determined flux distributions were then normalized and integrated from the ends to a cumulative value of 0.159 (i.e., corresponding to a  $1\sigma$  confidence limit).  $\sigma_C$  was adopted as half the range given by these two limits.

We found that all three terms of the variance,  $\sigma_\alpha^2(F - C)^2$ ,  $\alpha^2\sigma_F^2$  and  $\alpha^2\sigma_C^2$ , were comparable and necessary to have a full description of the emission line flux errors.

To increase the number of continuum measurements available for the variability analysis, we measured the mean value of the continuum in the 5620-7200 $\text{\AA}$  wavelength range from each spectroscopic observation, as a proxy for R-band photometric values. These ‘spectroscopic’ points were later scaled to the broad-band R-band photometry using a simple  $\chi^2$  minimization to bring the mean ‘spectroscopic’ light-curve in line with the photometric values.

R-band, Ly $\alpha$ , SiIV, CIV and CIII] light curves are presented in Figure 5 for all objects except for CT252, for which CIV, CIII] and MgII light curves are presented.

## CT650

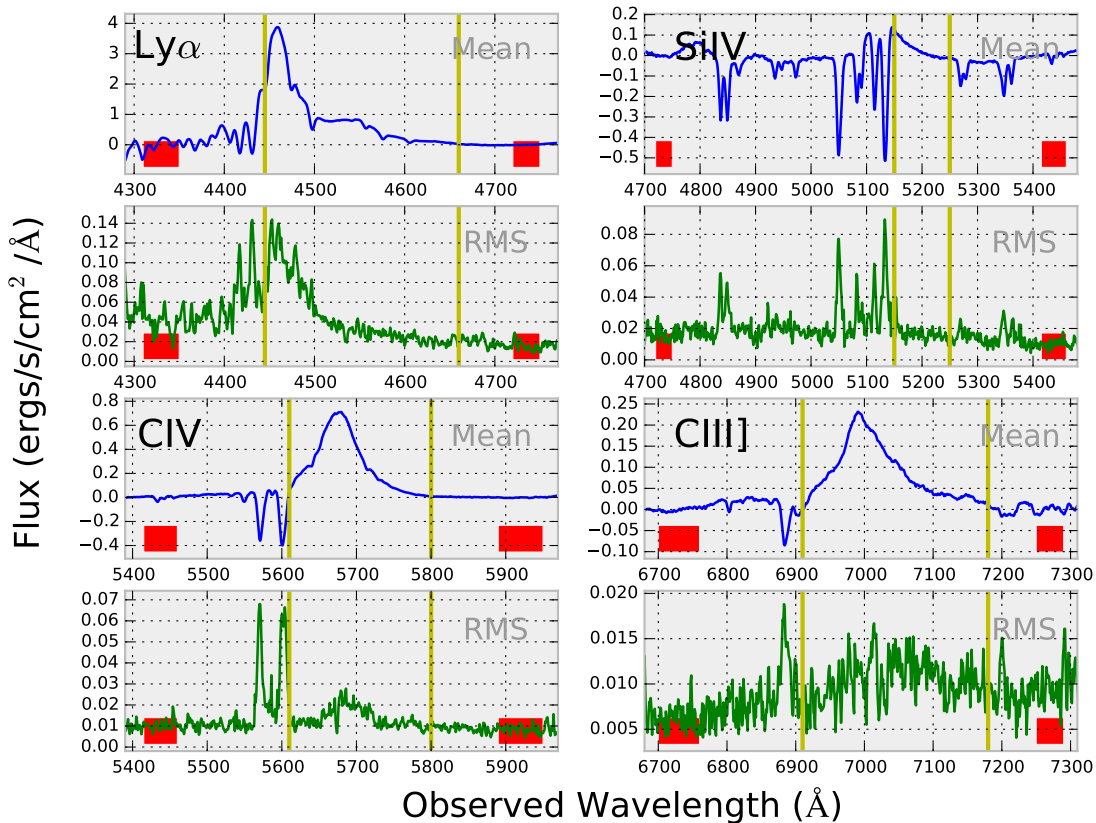


FIG. 3.— Mean (top panels – in blue) and rms (bottom panels – in green) spectra of CT650 around the Ly $\alpha$ , SiIV, CIV and CIII] emission lines. The mean spectra have been continuum subtracted using the continuum measurements obtained at the positions marked by red boxes. The line measurement is obtained as the summation of all flux between the vertical yellow lines.

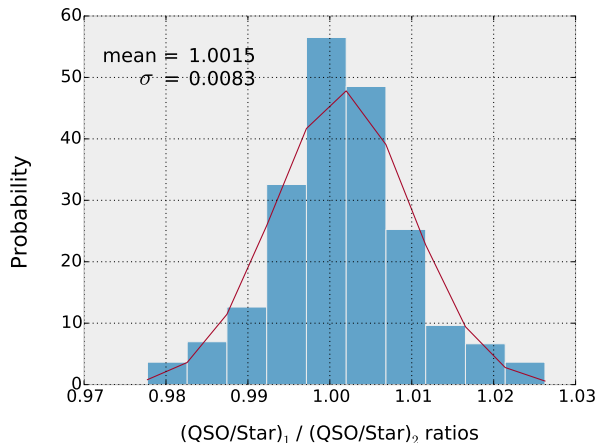


FIG. 4.— Distribution of Quasar/Star ratios.

The full database is found in the Appendix.

### 3. VARIABILITY ANALYSIS

#### 3.1. General continuum and emission line variability

Here we report on the  $\sim 10$ -year observer frame light curves for 17 quasars with spectroscopic follow up. The variability properties for these observations are reported

in Table 3. We list the number of epochs available (with the R-band counting both, the broad-band and spectroscopic continuum measurements),  $R_{max}$ , the ratio between the maximum and minimum flux,  $f_{var}$ , the normalized variability amplitude ( $\sqrt{(\sigma^2 - \delta^2)}/\bar{f}$ , where  $\delta$  are the photometric uncertainties,  $\bar{f}$  is the light curve mean flux and  $\sigma$  its standard deviation (Rodríguez-Pascual et al. 1997)),  $\chi^2$ , the reduced chi-square fit to a model with constant flux,  $P_\chi$ , the probability that the observed  $\chi^2$  is due to random errors, and cc indicates whether lag determination between emission line and continuum light curves was obtained (see Section 4). Formally, a source is considered variable if  $P_\chi > 0.95$  and  $\bar{f} > 0$ . Notice, however, that these statistical descriptions deal with the amplitude of the variability only, and not with the structure of the light curves as a function of time. In other words, while the errors in some light curves are consistent with no variations, the shape of the light curve might suggest a systematic flux change with time. This is particularly important for the emission line light curves, where errors are difficult to quantify properly. This can be appreciated, for example, in the Ly $\alpha$  light curve of CT1061 which has a  $P_\chi = 0.4$  and  $\bar{f} = 0$  but shows a clear trend of decreasing flux as a function of time.

From Table 3 it can be seen that all R-band light curves show significant variability and have  $P_\chi = 1.0$

TABLE 3  
LIGHT CURVE VARIABILITY STATISTICS

Quasar	l.c.	N	$R_{max}$	$f_{var}$	$\chi^2$	$P_\chi$	cc	Quasar	l.c.	N	$R_{max}$	$f_{var}$	$\chi^2$	$P_\chi$	cc
CT1061	Lya	13	1.05	0.00	0.8	0.30	y	CT803	Lya	21	1.15	0.02	2.0	1.00	n
	SiIV	13	1.12	0.00	0.1	0.00	n		SiIV	21	1.31	0.05	3.0	1.00	n
	CIV	13	1.10	0.01	1.4	0.83	y		CIV	21	1.15	0.00	0.5	0.04	n
	CIII]	13	1.20	0.00	0.6	0.14	n		CIII]	21	1.26	0.00	0.6	0.06	n
	R	65	1.32	0.08	56.8	1.00	–		R	79	1.47	0.08	50.3	1.00	–
CT250	Lya	17	1.22	0.05	11.9	1.00	y	CT953	Lya	23	1.35	0.07	11.4	1.00	y
	SiIV	17	1.54	0.00	1.0	0.58	y		SiIV	23	1.71	0.08	3.9	1.00	y
	CIV	17	1.39	0.06	4.7	1.00	y		CIV	23	1.27	0.05	5.4	1.00	y
	CIII]	17	1.40	0.03	2.0	0.99	n		CIII]	23	1.21	0.00	1.3	0.82	n
	R	67	1.47	0.11	81.1	1.00	–		R	74	1.61	0.12	592.3	1.00	–
CT252	CIV	17	1.25	0.07	34.4	1.00	n	CT975	Lya	17	1.20	0.03	1.6	0.94	n
	CIII]	17	1.10	0.01	1.3	0.78	n		SiIV	17	2.73	0.00	0.9	0.49	n
	MgII	17	1.49	0.09	15.6	1.00	n		CIV	17	1.33	0.05	2.4	1.00	n
	R	62	1.41	0.07	962.7	1.00	–		CIII]	17	2.70	0.12	2.8	1.00	n
CT286	Lya	23	1.20	0.04	8.8	1.00	y	HB89 0329-385	Lya	22	1.31	0.05	7.1	1.00	y
	SiIV	23	1.36	0.00	0.5	0.04	y		SiIV	22	1.91	0.00	0.9	0.43	y
	CIV	23	1.25	0.04	2.5	1.00	y		CIV	22	1.09	0.00	1.4	0.88	n
	CIII]	23	1.16	0.00	0.4	0.01	n		CIII]	22	1.21	0.00	0.9	0.40	y
	R	85	1.46	0.10	572.7	1.00	–		R	68	1.38	0.09	288.0	1.00	–
CT320	Lya	26	1.19	0.04	14.9	1.00	y	2QZJ002830	Lya	9	1.22	0.06	27.9	1.00	n
	SiIV	26	1.57	0.10	5.6	1.00	y		SiIV	9	1.53	0.11	5.9	1.00	n
	CIV	26	1.21	0.04	8.6	1.00	y		CIV	9	1.27	0.07	21.0	1.00	n
	CIII]	26	1.32	0.05	5.8	1.00	y		CIII]	9	1.14	0.03	2.0	0.96	n
	R	74	1.53	0.10	167.3	1.00	–		R	54	1.64	0.11	98.7	1.00	–
CT367	Lya	12	1.19	0.04	18.3	1.00	n	2QZJ214355	Lya	16	1.21	0.00	0.9	0.41	y
	SiIV	12	2.64	0.24	94.1	1.00	n		SiIV	16	1.33	0.00	0.5	0.08	n
	CIV	12	1.12	0.03	5.6	1.00	n		CIV	16	1.33	0.03	2.5	1.00	n
	CIII]	12	1.25	0.05	4.5	1.00	n		CIII]	16	1.60	0.00	0.3	0.00	n
	R	66	1.85	0.19	224.7	1.00	–		R	64	1.35	0.07	439.0	1.00	–
CT406	Lya	15	1.10	0.03	8.3	1.00	y	2QZJ221516	Lya	21	1.14	0.03	19.9	1.00	y
	SiIV	15	1.52	0.10	3.6	1.00	n		SiIV	21	1.56	0.05	1.2	0.78	n
	CIV	15	1.25	0.04	4.4	1.00	y		CIV	21	1.16	0.03	2.9	1.00	y
	CIII]	15	2.52	0.12	6.5	1.00	n		CIII]	21	1.36	0.00	0.9	0.43	n
	R	62	1.39	0.07	59.5	1.00	–		R	78	1.34	0.08	110.1	1.00	–
CT564	Lya	12	1.15	0.04	11.5	1.00	y	2QZJ224743	Lya	17	1.46	0.11	76.3	1.00	n
	SiIV	12	4.21	0.11	1.2	0.70	n		SiIV	17	1.52	0.11	12.5	1.00	n
	CIV	12	1.19	0.02	1.7	0.93	y		CIV	17	1.11	0.00	1.7	0.96	n
	CIII]	12	1.46	0.00	0.7	0.25	n		CIII]	17	1.20	0.01	2.1	0.99	n
	R	66	1.45	0.10	74.9	1.00	–		R	60	1.29	0.05	55.2	1.00	–
CT650	Lya	25	1.17	0.03	70.5	1.00	y								
	SiIV	25	7.66	0.29	13.8	1.00	n								
	CIV	25	1.14	0.03	41.4	1.00	y								
	CIII]	25	1.27	0.06	39.8	1.00	y								
	R	76	2.03	0.15	176.7	1.00	–								

and  $\bar{f} > 0$ . Still, there is a range of properties in the variability structure, with some sources presenting very smooth, slowly varying fluxes (e.g., CT367) while others go through epochs of a more random, fast changing fluxes (e.g., CT320).

Most emission line light curves present significant variability. Adopting  $P_\chi \geq 0.95$  for variable light curves, 15/17 quasars show large Ly $\alpha$  flux fluctuations. CIV follows with 12/17, SiIV with 10/17 and CIII] with 12/17 (plus MgII with 1/1 for CT252). In summary, we find that Ly $\alpha$  presents a very high probability of showing strong variability. This is in contrast with previous results that detected no variations in this line for high luminosity sources (Kaspi et al. 2007, Ulrich et al. 1993). CIV is also a highly variable line, followed by SiIV and CIII]. This is expected as these lines are generally weaker and therefore it becomes harder to determine statistically significant variations. It should be noticed, however, that

our spectroscopic sample was selected as those quasars that showed significant R-band variability, and therefore it could be biased towards highly variable sources. Comparison with previous experiments, might therefore, not be very meaningful.

In what follows we divide our sample into two groups: a first group with ‘expected’ line variability (14/17), i.e., those showing emission line light curves that agree with the expectations given the continuum variations, and a second group of those objects with detected line variability that seems to respond to the continuum changes in unexpected ways (3/17).

### 3.2. Quasars with expected line response

Most of the monitored quasars show some degree of line variation that mimics the continuum variability after some elapsed time (see left panels in Figure 5). This is crucial for the cross correlation analysis presented in



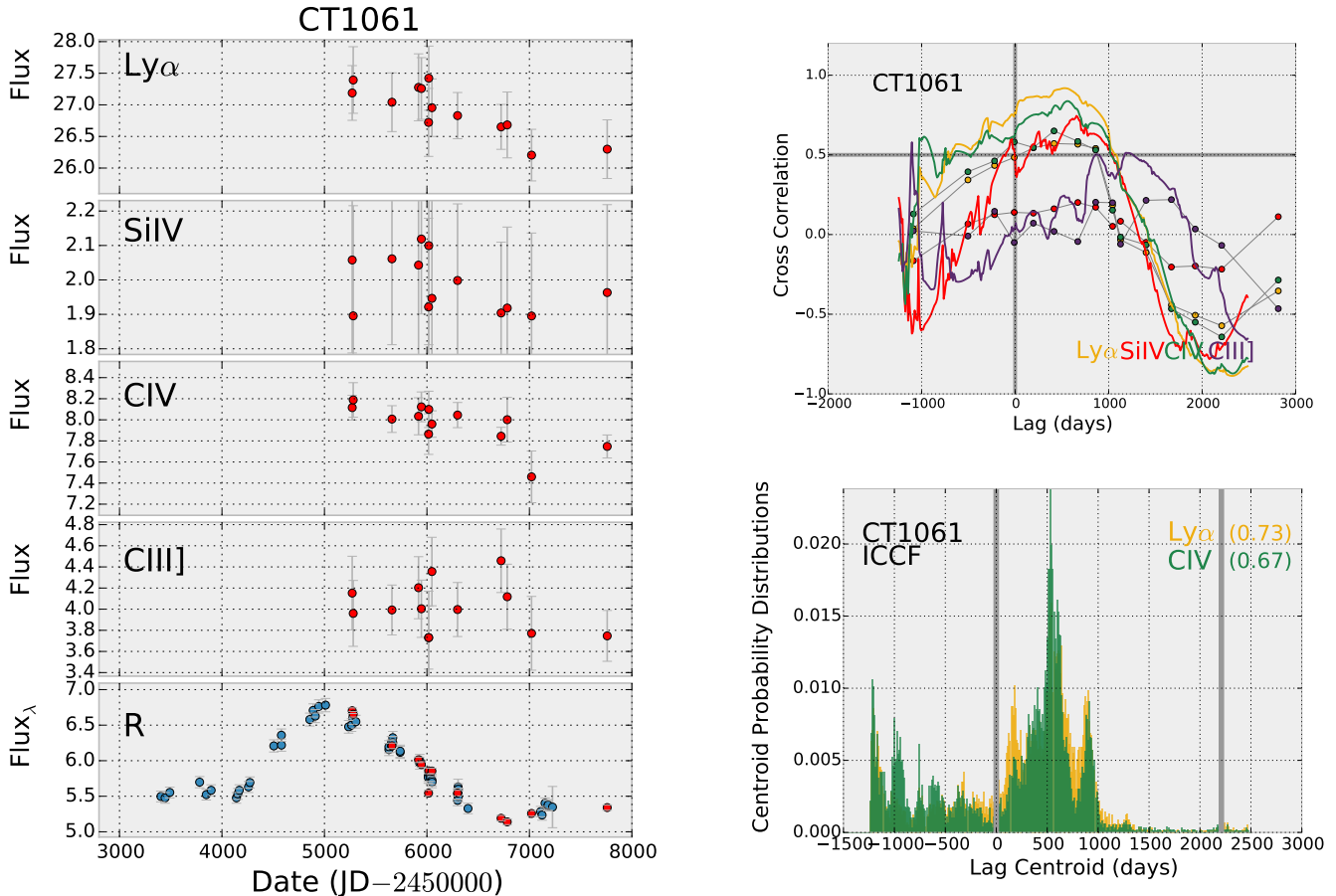


FIG. 5.— **Left:** Line and continuum light curves for all quasars with spectroscopic follow-up. Red points correspond to measurements taken from the spectroscopic data, while blue points correspond to broad-band R photometry. Units are  $10^{-14}$  erg  $s^{-1}$   $cm^{-2}$  for the line measurements and  $10^{-16}$  erg  $s^{-1}$   $cm^{-2}$   $\text{\AA}^{-1}$  for the R-band light curves. **Right, top panels:** correlation functions obtained using the ICCF (continuous line) and ZDCF (points) methods for the Ly $\alpha$ , SiIV, CIV, and CIII] emission lines. **Right, bottom panels:** Cross Correlation Centroid Distributions (CCCDs) obtained from the ICCF FR/RSS analysis for those lines with significant peaks in their ZDCF and ICCF correlation functions. Thick gray lines show the limits of the distributions used for lag error determinations. The fraction of the CCD contained within the thresholds is shown in parenthesis for each line. For further details, see the text.

Section 4, as quasars in this group show good indication that the emission lines are reverberating as a response to variations in the continuum. Unfortunately, some sources in this group present rather monotonic flux variations (CT367, CT803, J002830) and therefore the present light curves are not suitable for cross-correlation analysis. This will be further characterized in Section 4.

### 3.3. Quasars with unexpected line response

We find three quasars where the lines response to the continuum variations are hard to interpret. These are CT320, CT803 and J224743.

In all sources one of emission lines seems to have disengaged from the observed continuum, while the remaining lines show a pattern of variability more consistent with the R-band light curve. In the case of CT320, the anomalous behavior is observed in SiIV, while for CT803 and J224743, it is observed in Ly $\alpha$ . As we will see in Section 4, very little correlation is observed in the cross-correlation analysis of the light curves in these emission lines.

The most likely explanation for the lack of correlation between continuum and line emission light curves is that in these objects the *observed* continuum is not a

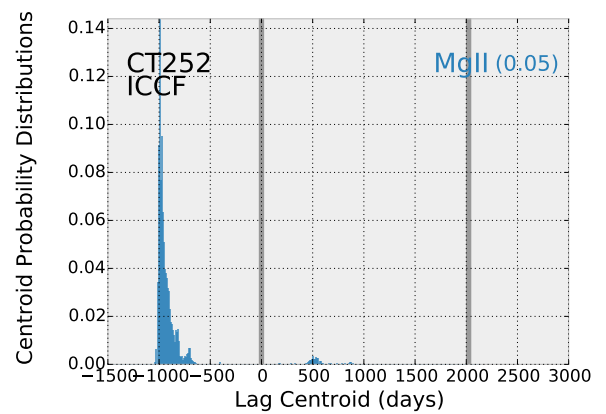
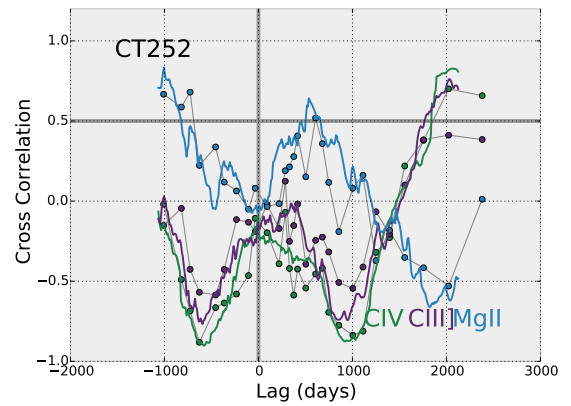
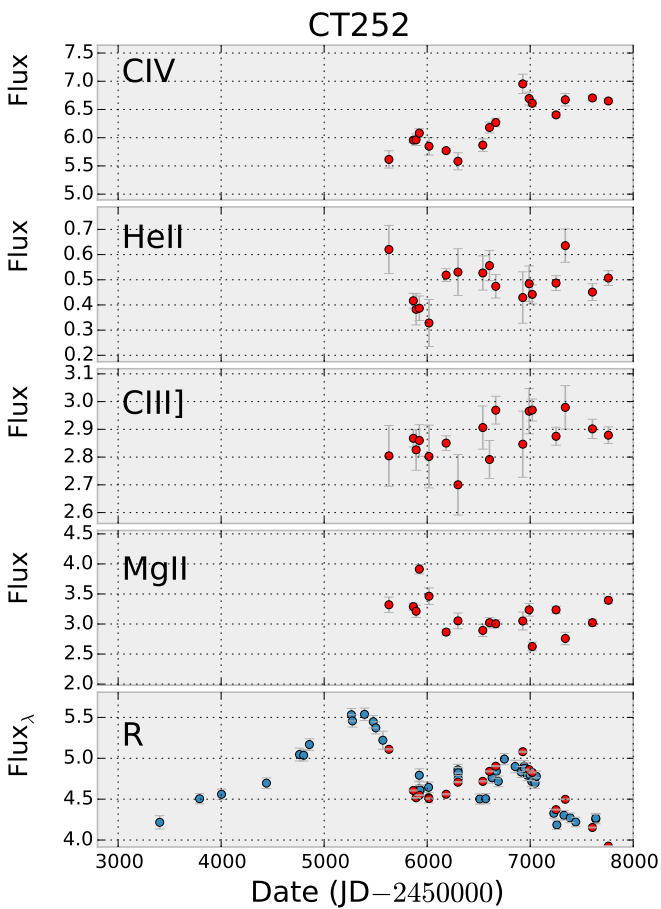
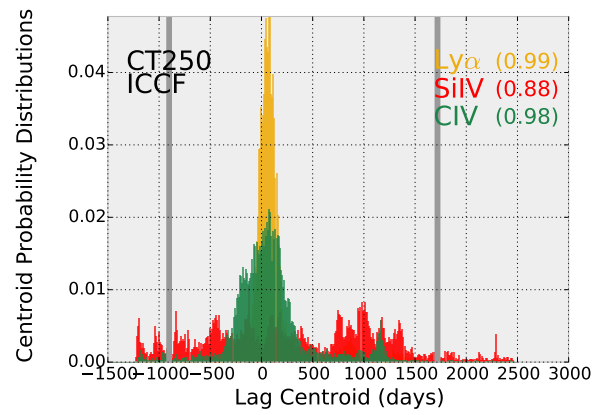
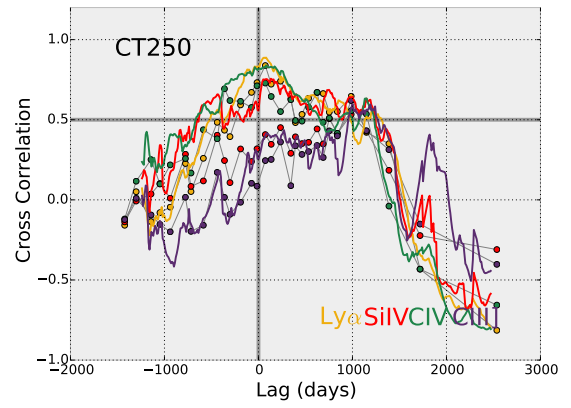
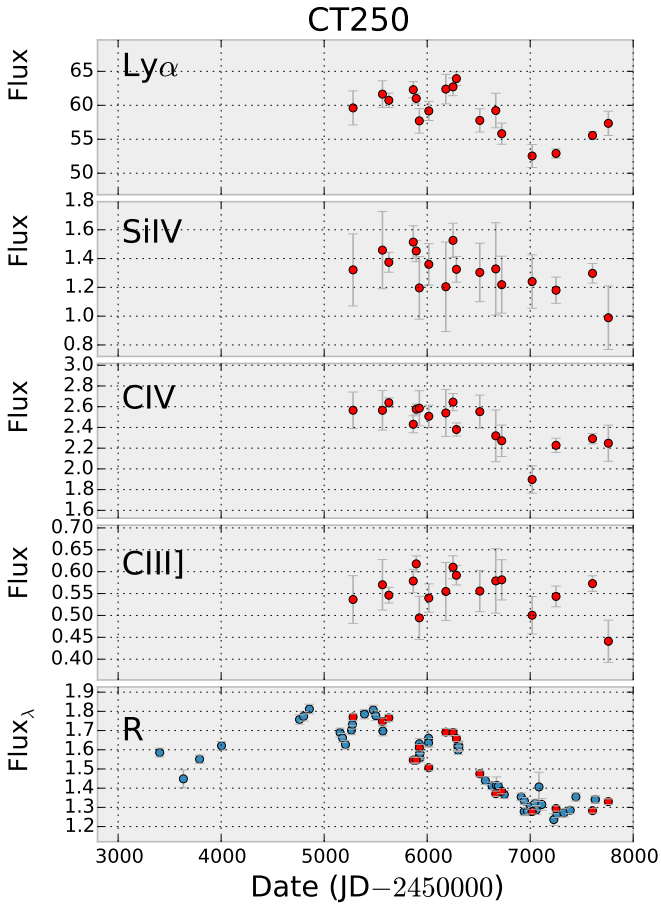
good counterpart of the ionizing continuum responsible for the observed line variations. This is not completely unprecedented, as we will further see in the discussion section.

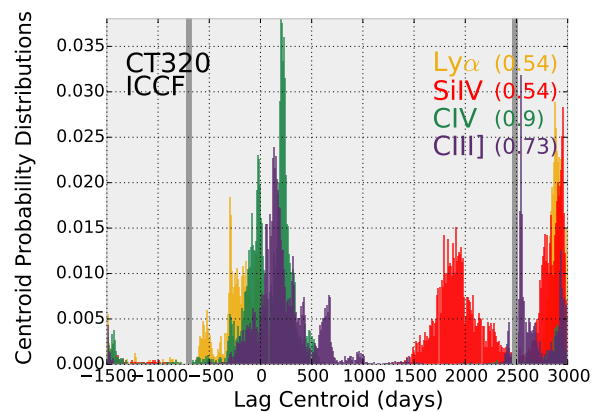
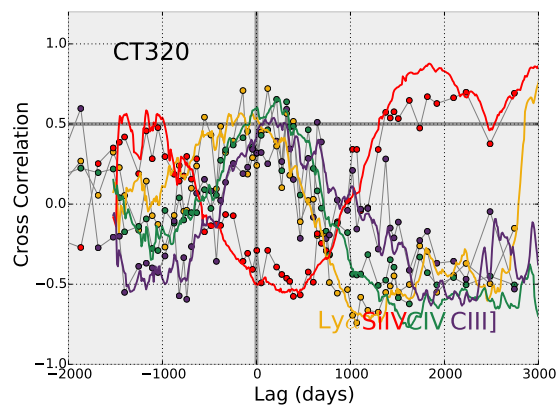
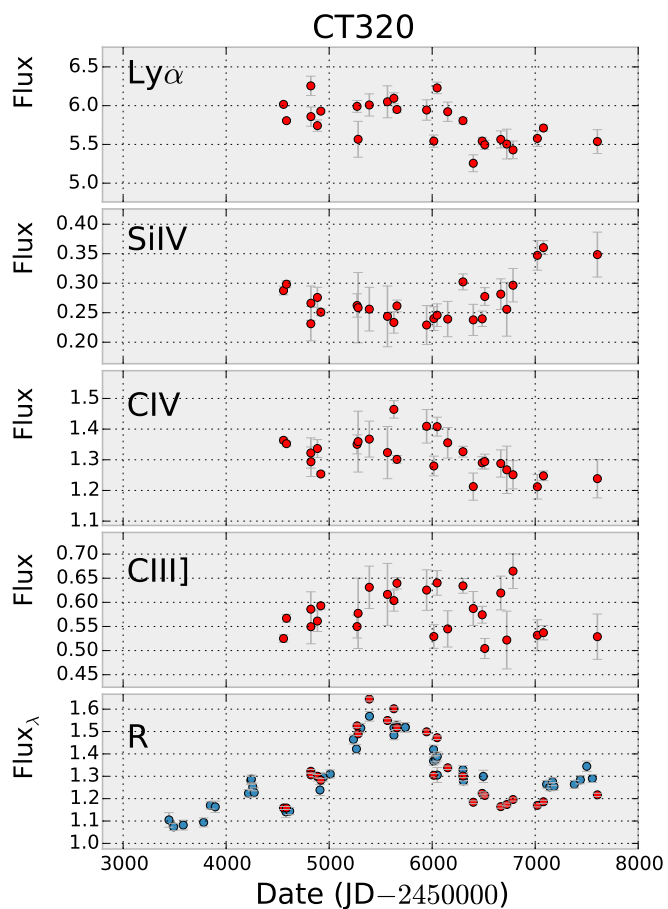
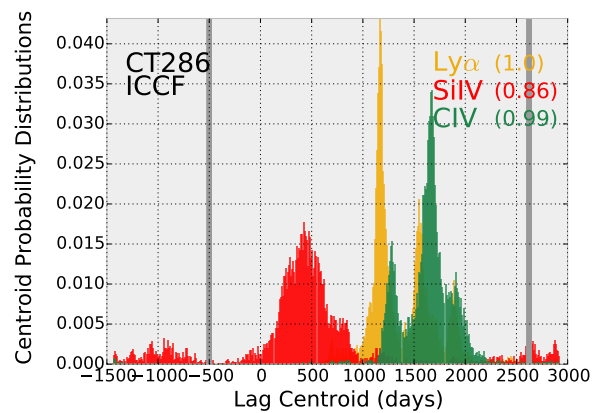
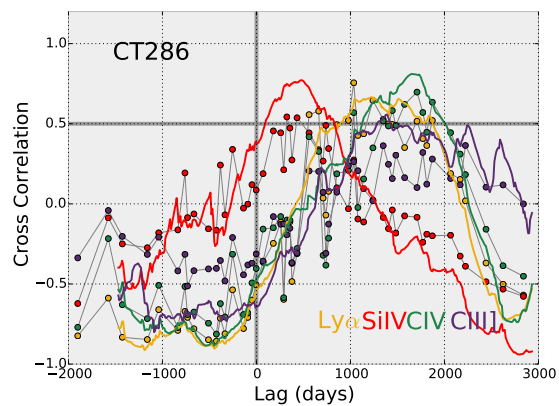
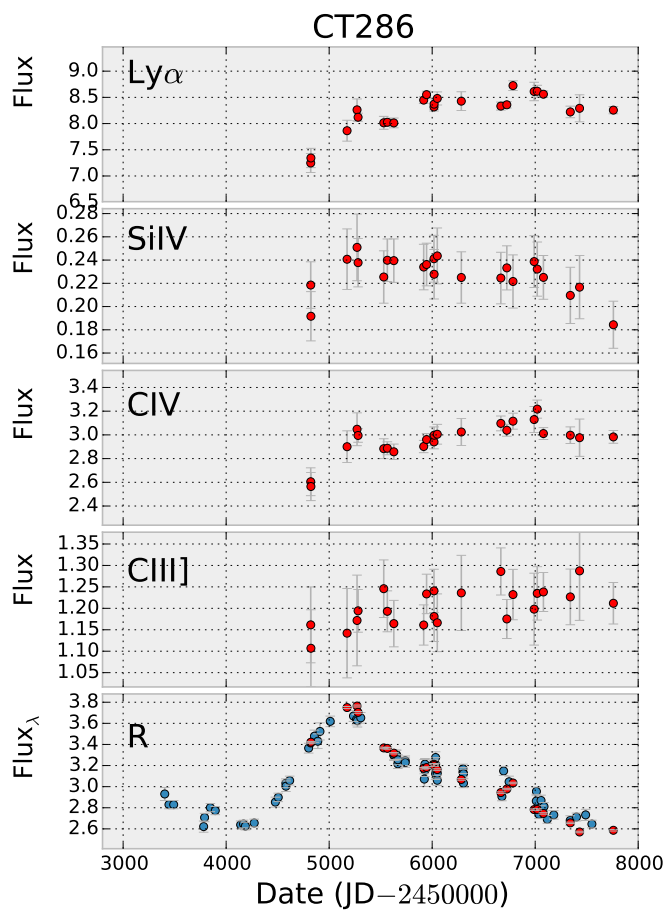
## 4. CROSS CORRELATION ANALYSIS

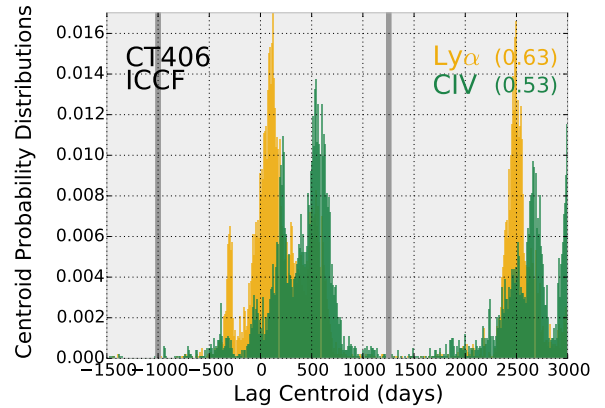
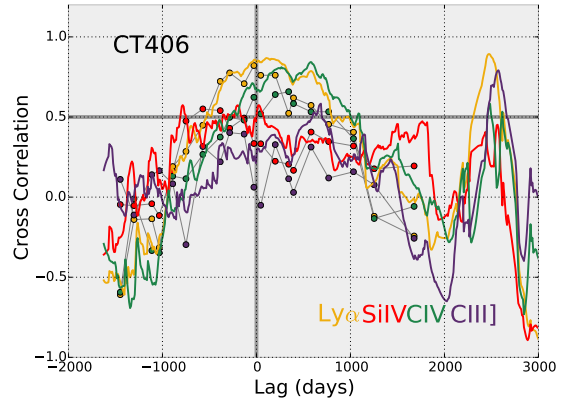
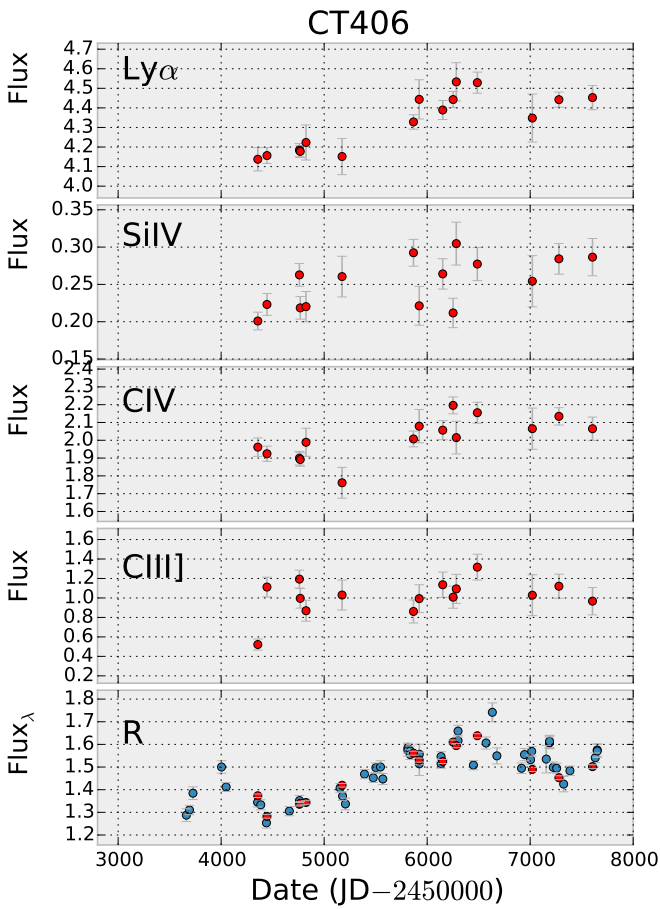
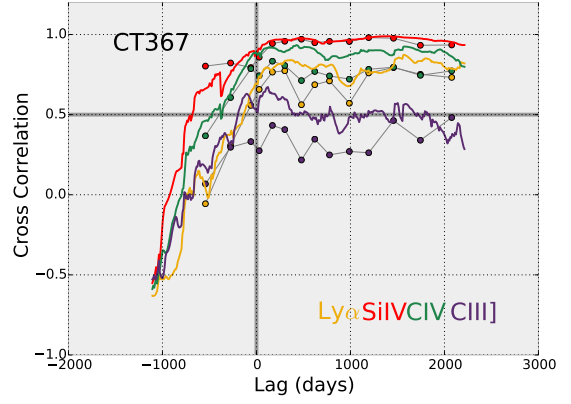
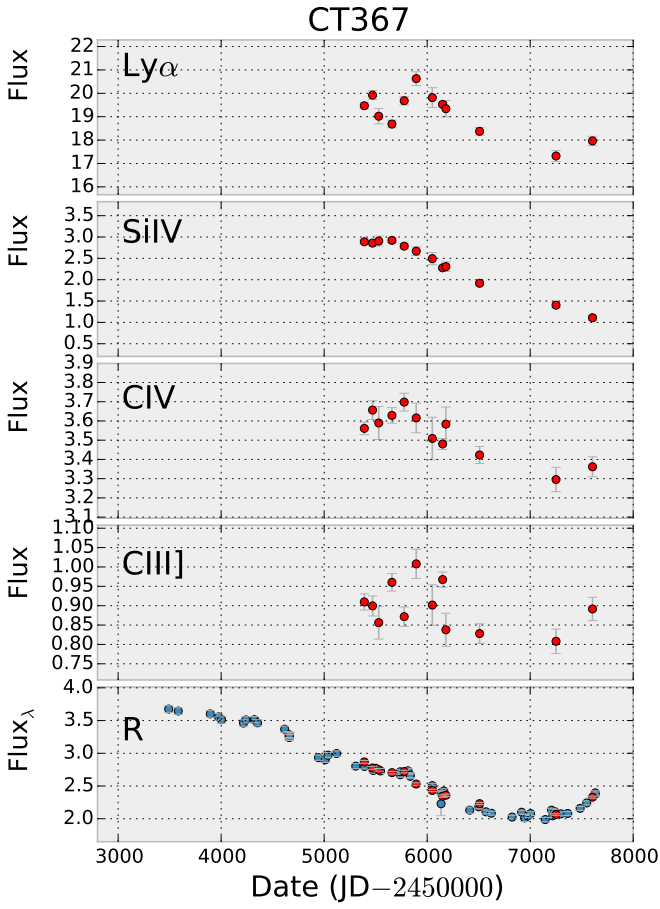
Cross correlation functions (CCFs) for all our targets with spectroscopic data were determined. All emission line light curves are used, irrespective of their  $P_{\chi}$  values, since as we have seen, this quantity does not reflect the structure of the variability.

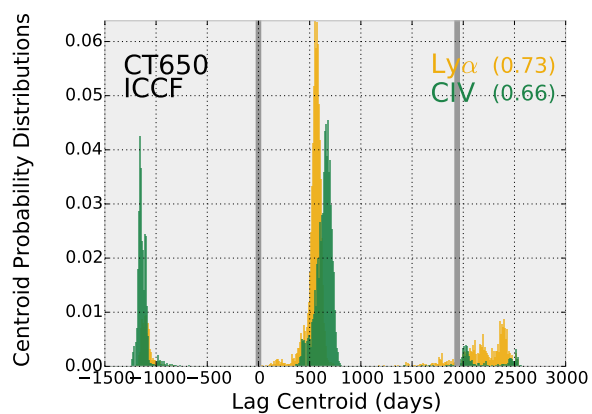
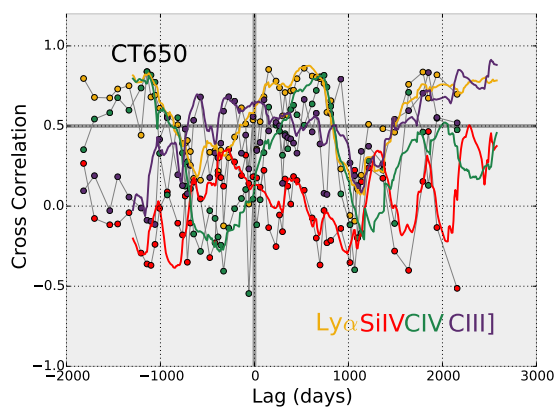
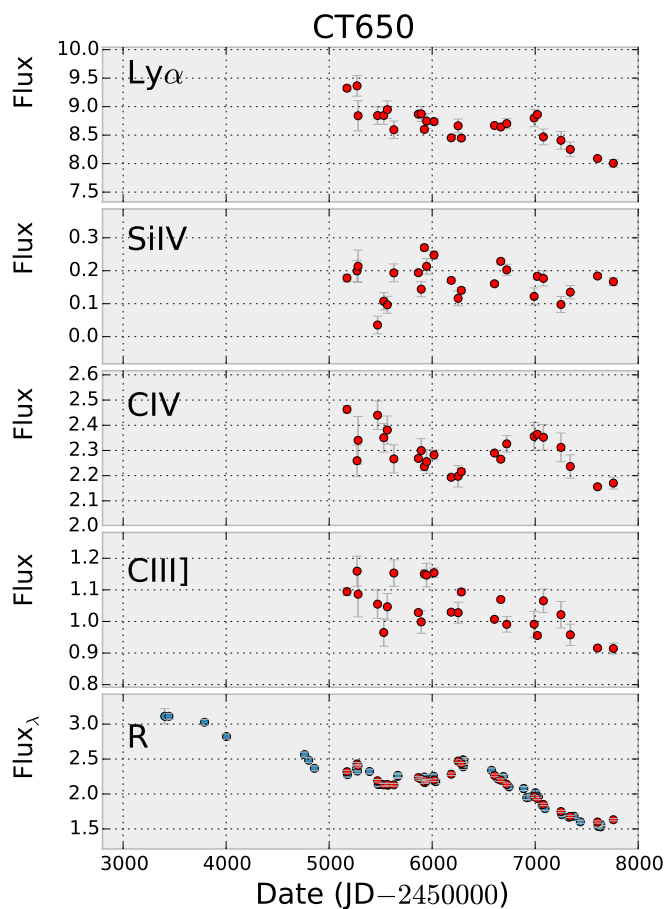
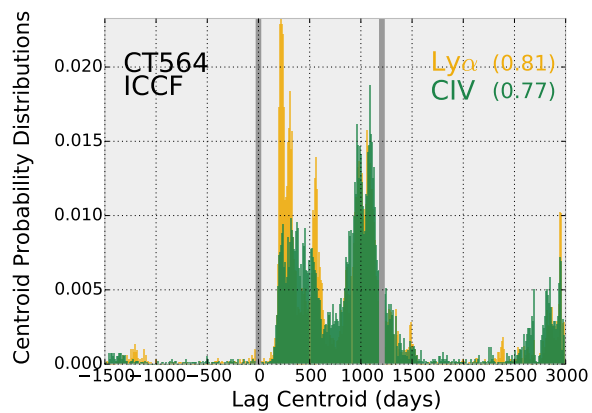
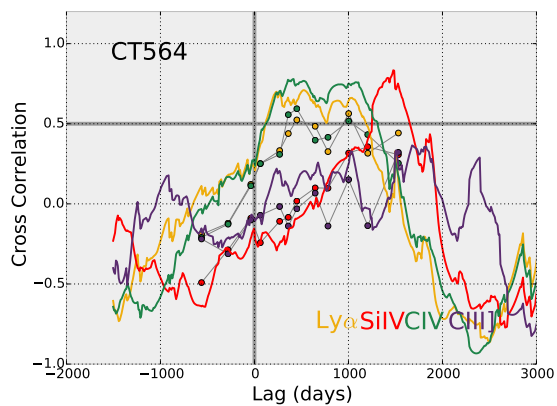
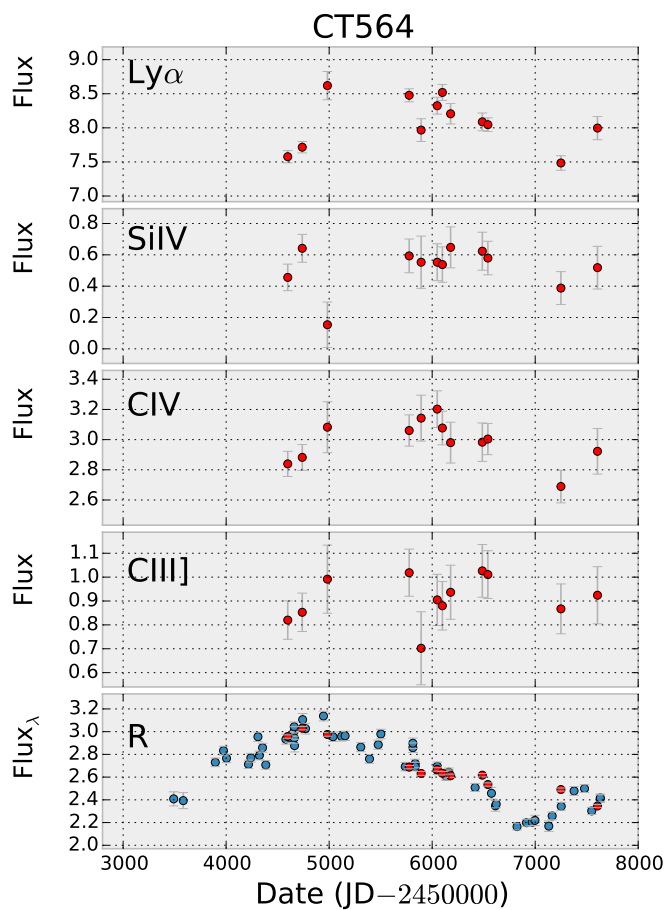
Three methods were employed to examine the degree of correlation between the continuum and emission line light curves: the interpolated cross correlation function (ICCF, e.g., Peterson et al. 1998, 2004), the z-transformed discrete correlation function (ZDCF) as defined by Alexander (1997), and the JAVELIN method described by Zu et al. (2011, 2013). We will discuss cross correlation results for the ICCF and ZDCF methods first, which are presented in the top-right panels of Figure 5, and later comment on the JAVELIN findings.

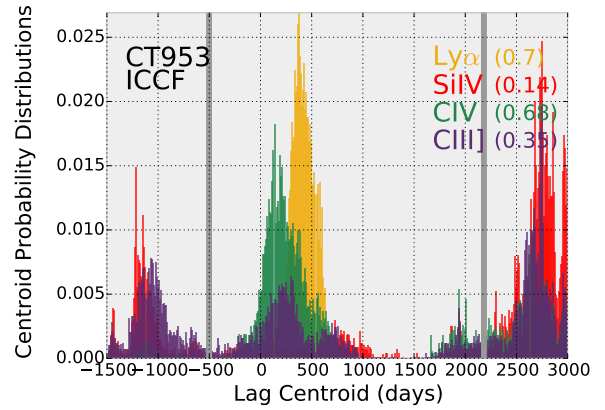
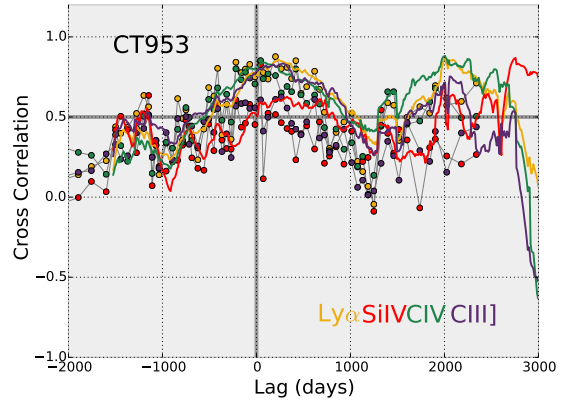
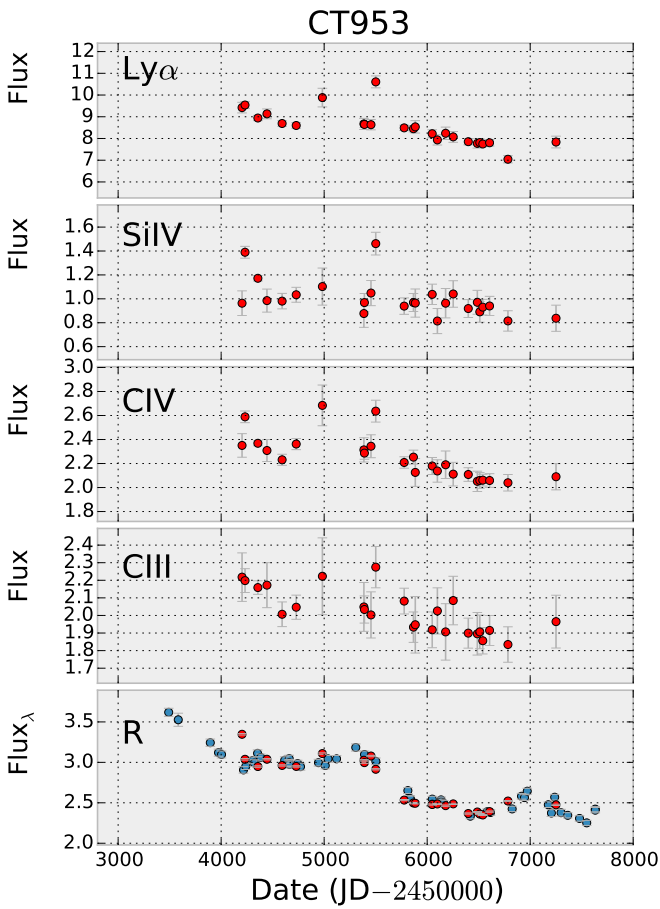
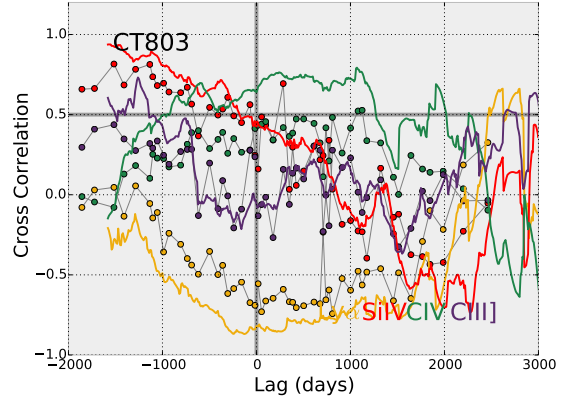
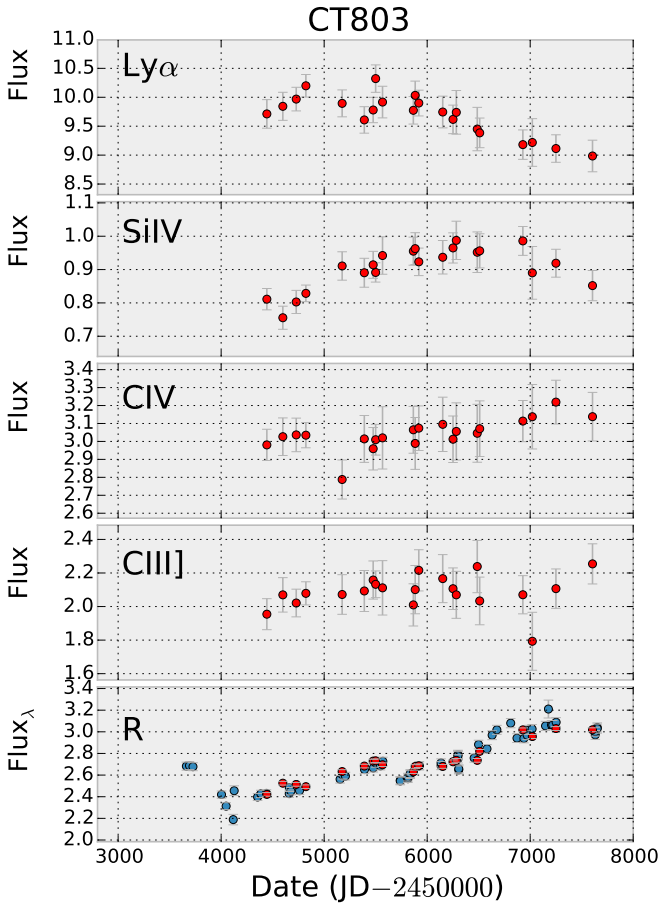
The ICCF determines the maximum of the CCF between light curves after interpolating fluxes to a desired cadence. The assumption used is that the line and con-

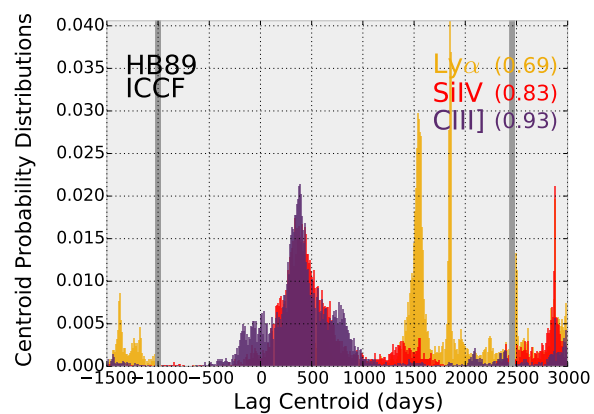
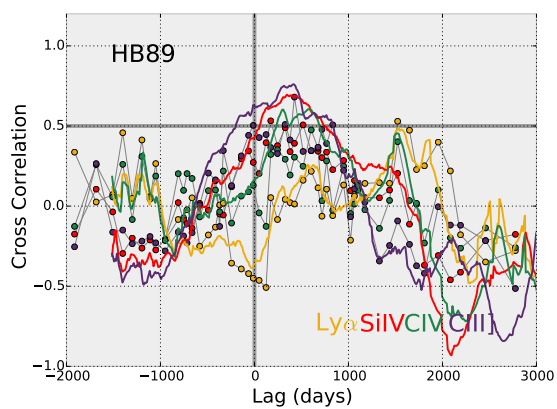
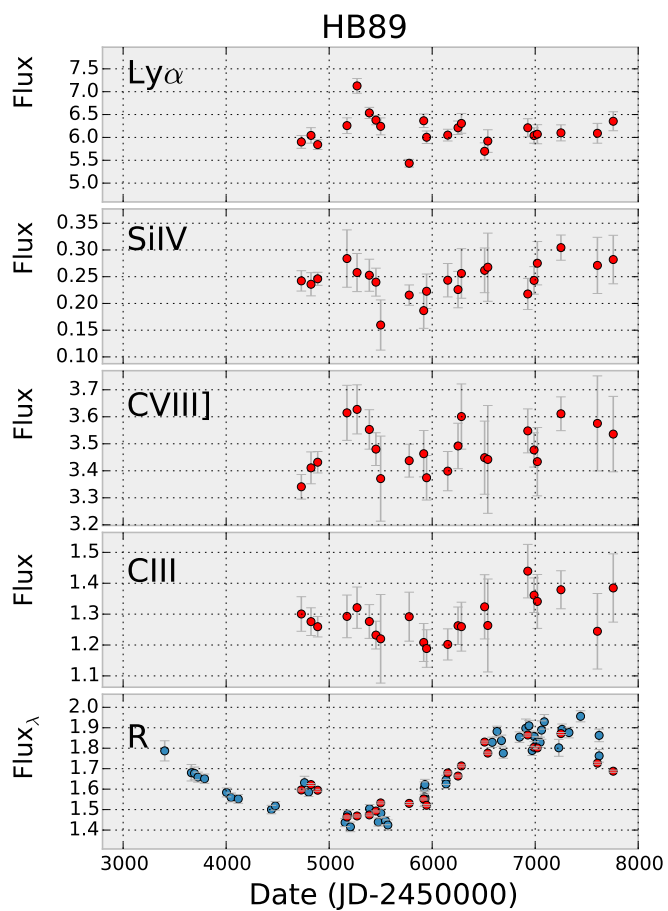
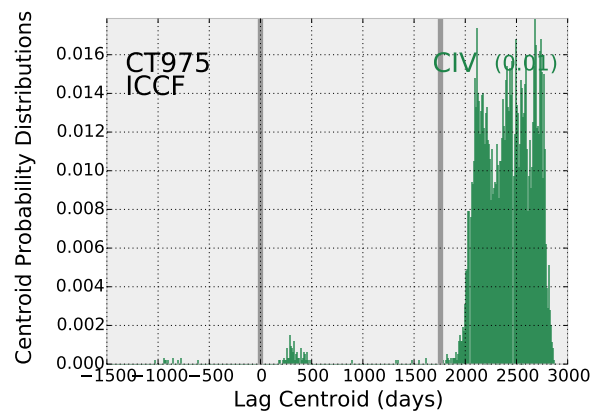
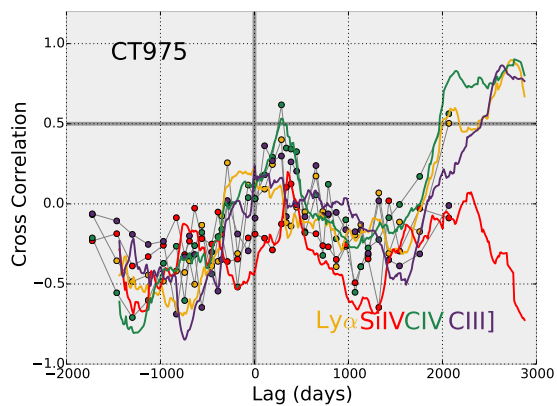
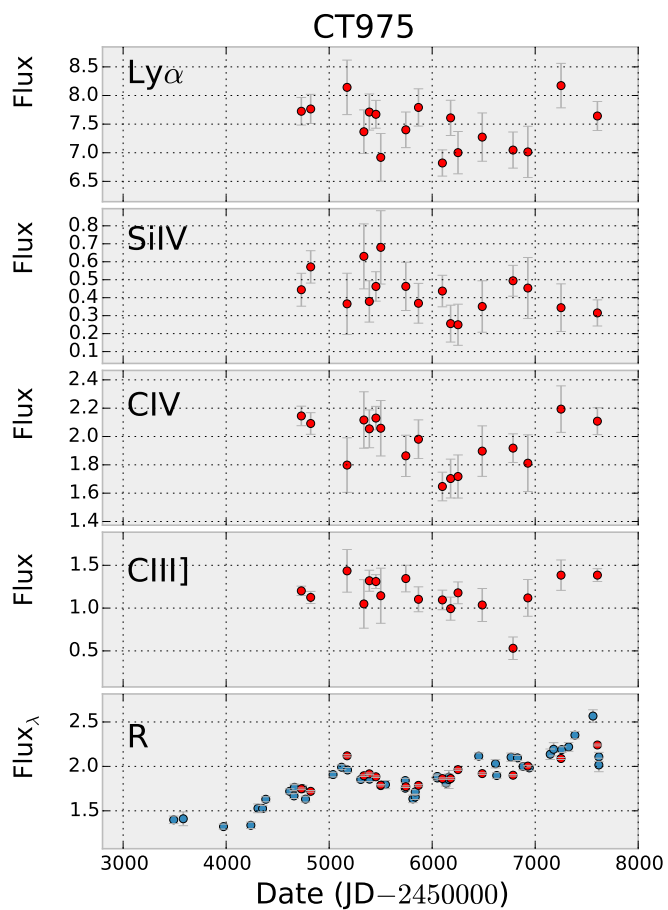


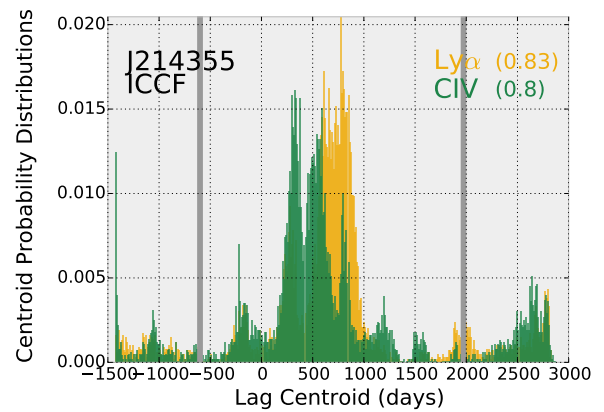
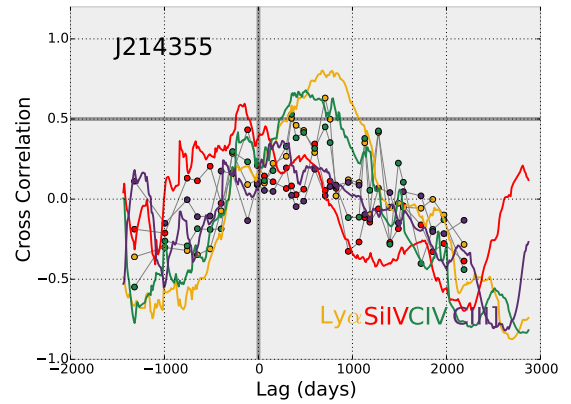
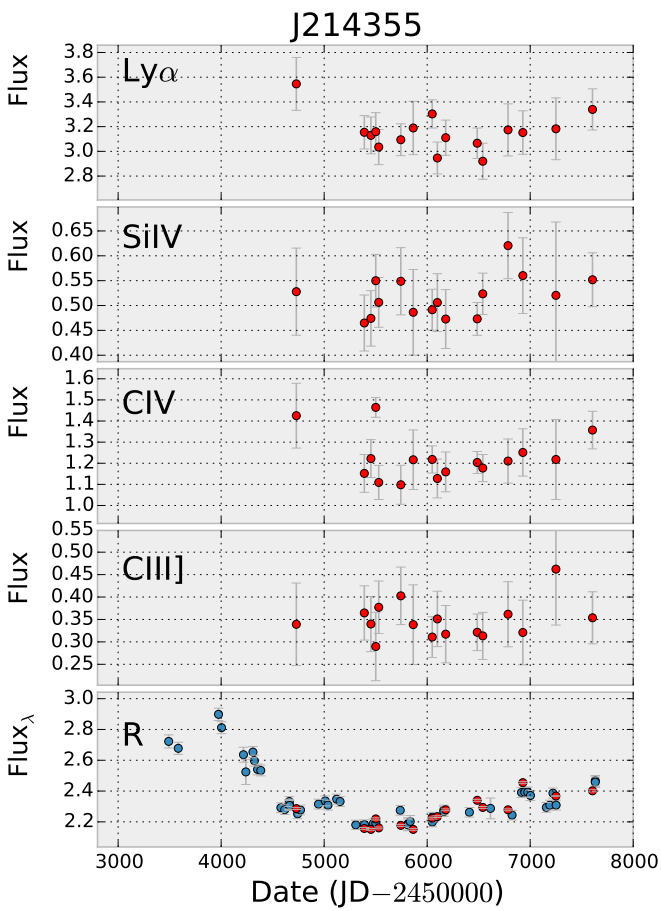
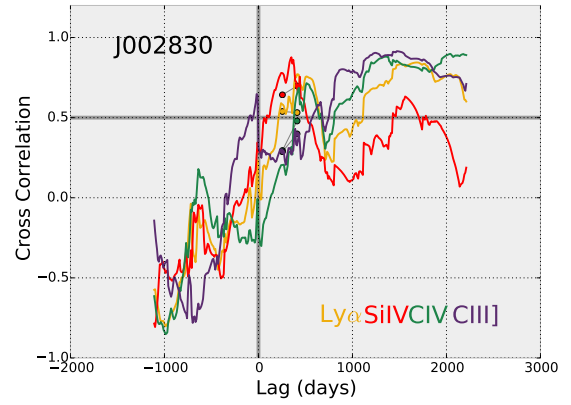
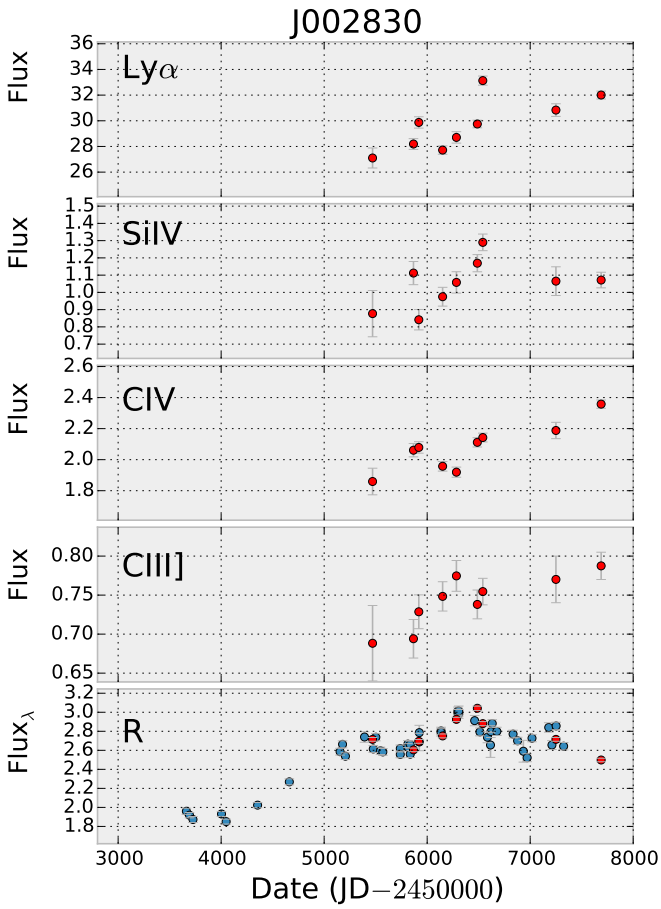




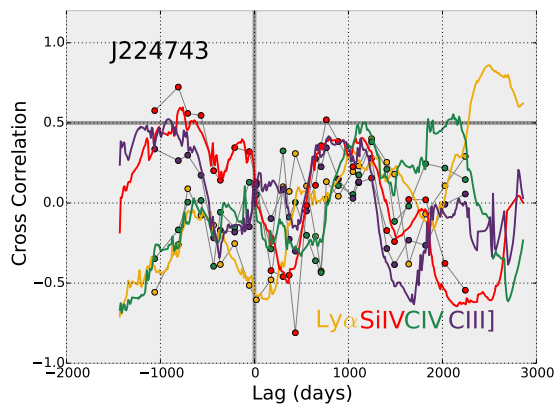
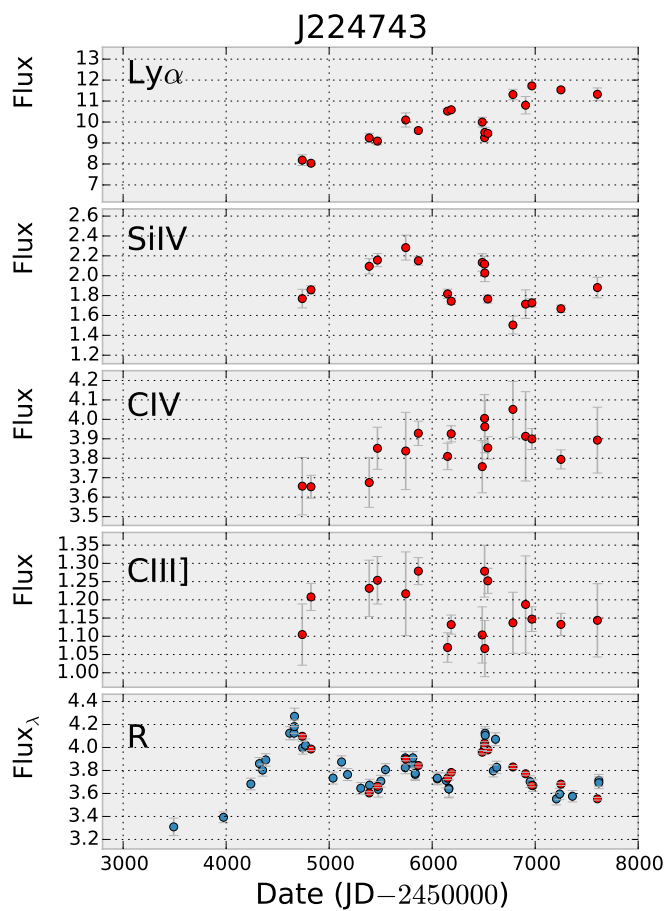
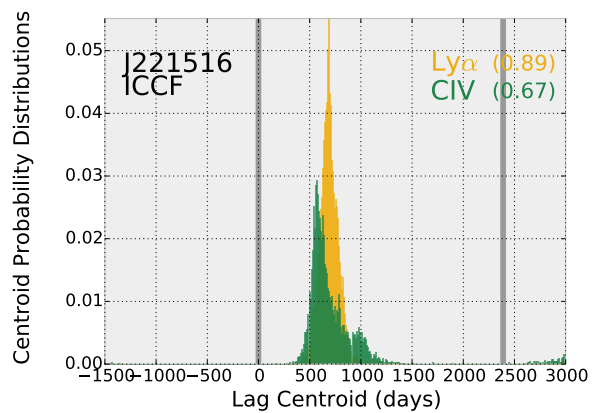
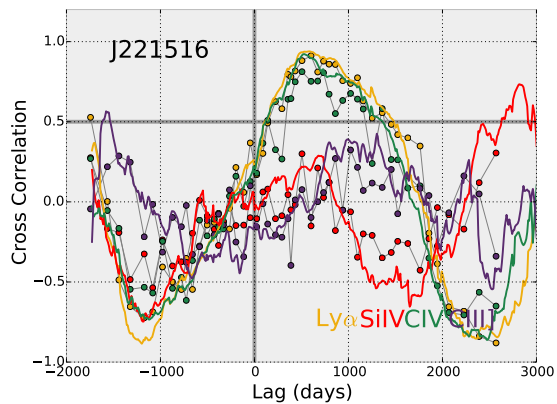
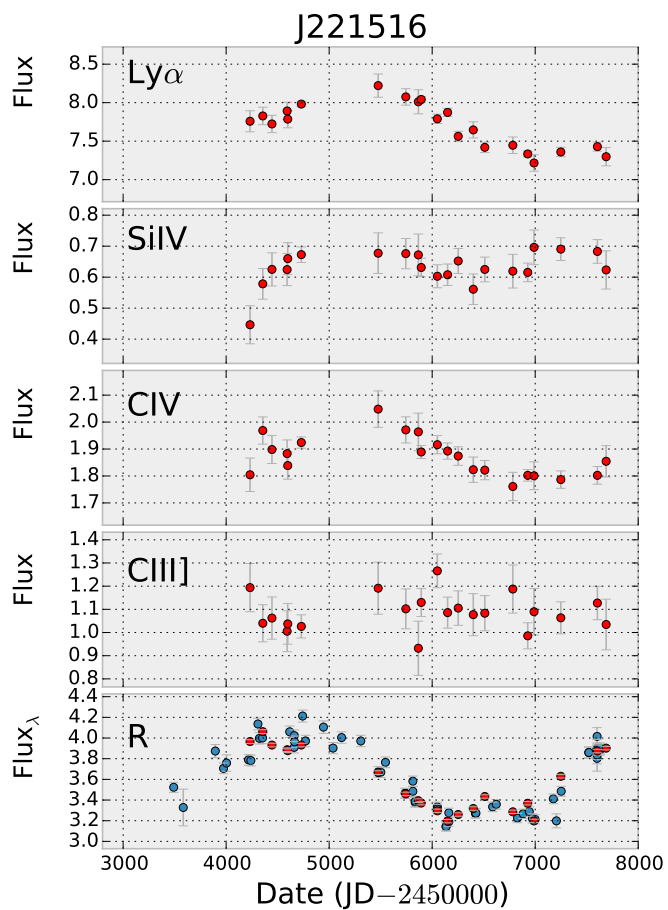












tinuum fluxes in gaps between two observed points are properly approximated by a linear interpolation in time between the two (see e.g., Peterson et al. 2004 and references therein). For our sample, the ICCF was run for a cadence of 10 days and between  $-s/2$  and  $s$  days, where  $s$  is the time span common to the continuum and each emission line light curve.

Of the three cross correlation methods described here, ZDCF is the only one that works solely with the *observed* values of the light curves. It is based on the discrete correlation function (DCF) of Edelson & Krolik (1988) which uses the available data without resorting to interpolation, hence not altering the observed light curves. The DCF method bins the time difference pairs and obtains the mean correlation coefficient for each bin. A minimum of 11 points is required in each bin, which determines the length of the correlation, except for the two bins at the edges where a smaller number of points is allowed. The ZDCF introduces a ‘z-transformation’ of the DCF correlation coefficient in order to avoid the inherent skewedness of the DCF parent distribution function.

Inspection of the correlations presented in the top-right panels of Figure 5 shows that in some cases the ICCF and ZDCF follow each other closely (e.g., Ly $\alpha$  and CIV in CT250), while in other cases there are significant differences (e.g., SiIV in CT250 and all lines for J214355), with the ICCF showing higher correlation coefficients than the ZDCF. This is due to the ‘extra’ information introduced by the interpolation technique. Also, in some cases the ICCFs are more extended than the ZDCF (e.g., CT406), because of the requirement of a minimum number of points per bin by the ZDCF. In other words, those regions where the ICCFs extend further than the ZDCF correspond to regions of sparsely sampled light curves. In summary, ZDCF results give a more conservative inference of the correlation strength.

Given the above differences between the methods, we will only consider those emission line light curves that have ICCF and ZDCF cross correlation coefficient distributions agreeing with each other, and a well defined peak for positive lags above a cross correlation coefficient of 0.5 (this is, at least one ZDCF point above 0.5 which is part of a coherent peak seen in the ZDCF; usually the ICCF will be found at even higher correlation coefficient levels). We treat negative peaks as failure to determine physical meaningful lags, although different explanations, involving a whole different view of the central region of AGN, could also be considered. Hence, the peaks to be considered should be found in the upper-right quarter of the top-right panels in Figure 5. For example, we will consider the Ly $\alpha$  and CIV light curves for CT1061, but drop the SiIV and CIII] light curves of this source.

Following these criteria, we drop CT252, CT367, CT803, J002830, and J224743 from any further analysis. For the remaining sources not all emission lines will be considered. This is indicated in Table 3.

To estimate the lags, the maximum of the ICCF can be determined in two ways: finding the peak (or maximum value) of the ICCF (for positive lags and cross correlations coefficients larger than 0.5), and finding its centroid (or weighted mean) around the peak above a certain threshold value. As centroids are more reliable than peaks in flat or noisy ICCFs, in what follows we adopt the centroids ( $\tau_{cent}$ ) as the measured lags for those

sources showing significant ICCF and ZDCF peaks, as discussed above. In our case, for the determination of  $\tau_{cent}$ , a threshold of 0.85 times the maximum was used.

To determine the lag associated errors, we followed the usual flux randomization and bootstrapping Monte Carlo technique (also known as FR/RSS), using a code facilitated by B. Peterson. Briefly, ICCFs are computed from light curves constructed after fluxes are randomized within the observed errors (Flux Randomization – FR) and 70% of points are selected from the observed sequences (Random Subset Selection – RSS) – for more details see Peterson et al. (1998, 2004). 10000 such trials were obtained. As before, the trials had a cadence of 10 days and run between  $-s/2$  and  $s$  days. With all successfully determined centroids, a Cross-Correlation Centroid Distributions (CCCDs) for objects showing significant ICCF and ZDCF peaks are presented in the bottom-right panels in Figure 5.

CCCDs in Figure 5 show a wide range of morphologies with sometimes more than one peak of high statistical probability. This is in contrast with the CCCDs obtained for many well monitored Seyfert galaxies, since the presence of many variability ‘events’ helps to constrain the lags to a singular, well defined peak (e.g., see Clavel et al. 1991, Wanders et al. 1997, Peterson et al. 2005, Edelson et al. 2015, Fausnaugh et al. 2016). This degeneracy in the possible lags seen in the bottom-right panels in Figure 5 cannot be unambiguously solved unless the light curves could be dramatically extended in duration. However, it is clear that the observed secondary peaks are found at the same locations where unfeasible peaks were also observed in the ICCF-ZDCF distributions shown in the top-right panels in Figure 5 (i.e., regions where the number of ZDCF points is small and hence the ICCF interpolation not very meaningful; see below) Therefore we can use the same arguments as before to dismiss them.

For the lag error determinations we truncated the CCCDs at a minimum and maximum lag and renormalized. The criteria were to leave out complete peaks that implied negative lags (which are unfeasible), while negative wings of positive lags were still taken into account. The upper threshold was given by the largest time bin computed by the ZDCF algorithm before the final bin (which usually has less than 11 measurements), i.e., before the light curves become too sparse for meaningful interpolation and lag determinations. These thresholds are shown in Figure 5 using vertical gray lines. Lag errors were finally computed as a  $1\sigma$  confidence limit range by integrating the re-normalized CCCDs from the determined thresholds until a cumulative value of 0.159 was reached on each end, which determines  $\sigma_-$  and  $\sigma_+$ . A final criterion to consider a lag as reliable is imposed at this stage, with the requirement that at least 50% of the original CCCD is found within the defined thresholds (see also Grier et al., 2017). This fraction is shown in each CCCD presented in Figure 5. This restriction leaves out the MgII lag for CT252, the CIII] lag for CT953, and the CIV lag for CT975. As before this is indicated in the ‘cc’ column in Table 3. Table 4 presents the final list of lags and their error estimates. The MgII lag for CT252, CIII] for CT953, and CIV for CT975 are also included in Table 4 but not used for further analysis.

We also used JAVELIN to characterize the observed lags (Zu et al. 2011, 2013). JAVELIN models the light

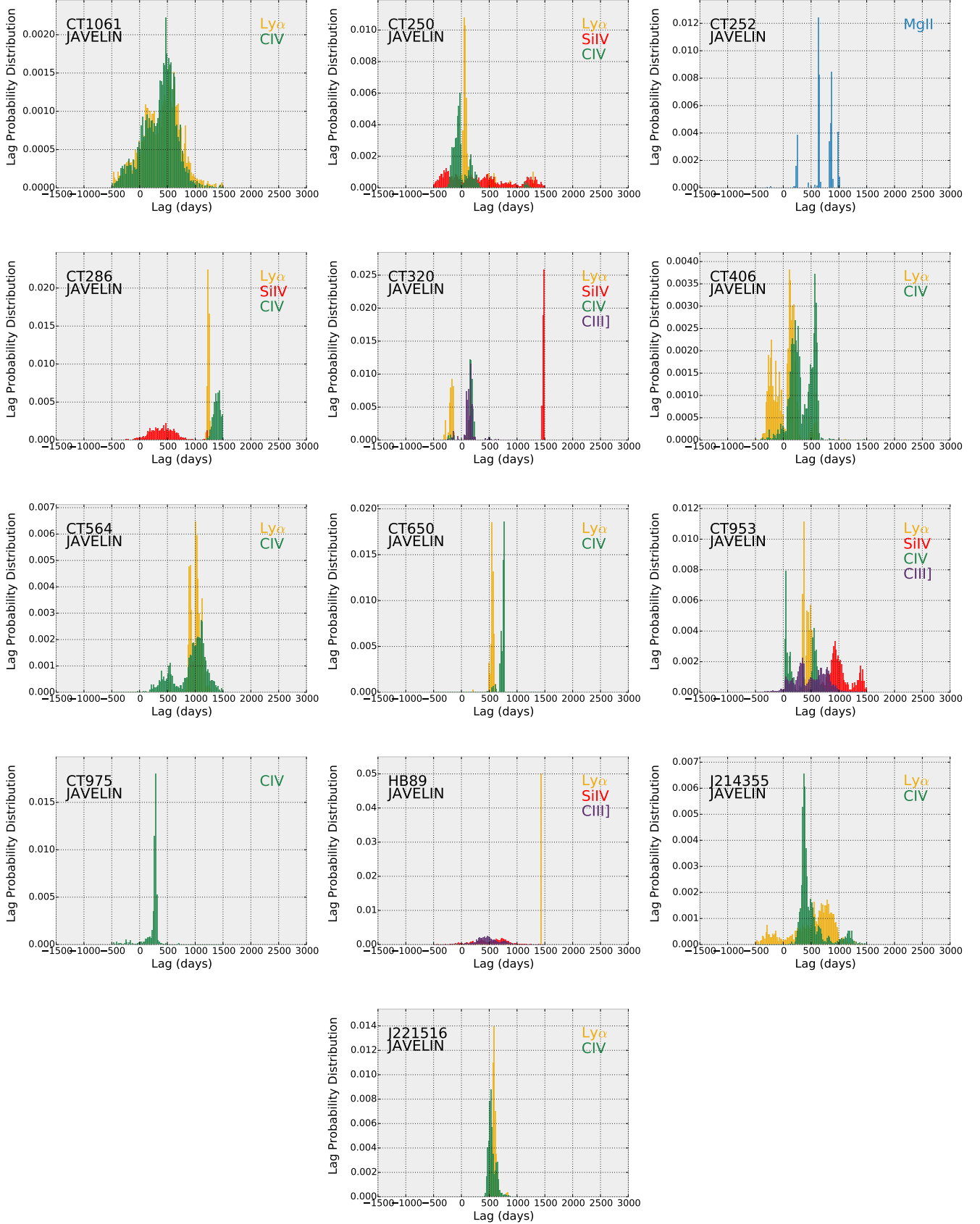


FIG. 6.— Lag Probability Distributions from the JAVELIN analysis.

curves as a damped random walk process (DRWP, also called purely Auto-Regressive, AR(1), process) as prescribed by Kelly et al. (2009), i.e., assumes a particular regime of the power spectral function (with  $P_\nu \propto \nu^\alpha$  with  $\alpha = -2$ , breaking to  $\alpha = 0$  at a characteristic frequency) in order to determine a lag and its significance.

The advantage of JAVELIN over the ICCF method is that the errors associated to values interpolated between actual observations are based on the DRWP model, which are usually larger and more realistic than those obtained from a linear interpolation. However, for sufficiently well sampled light curves, it has been found that a DRWP model only applies to about half of AGN of Seyfert and quasar-like luminosities (Kasliwal et al. 2015). Moreover, the basic assumption of JAVELIN is that the emission line light curves are the result of the response to an ionizing continuum which is changing exactly in the same way as the observed continuum used in the calculations, in contradiction to some well documented previous results (Goad et al. 2016), as well as some of the cases presented in this work. In fact, JAVELIN computes a solution which assumes a transfer function of the continuum and solves simultaneously for both, the continuum and line emission interpolated light curves.

We run JAVELIN using the same lag limits used during the ICCF calculations, implemented 5000 Markov chain Monte Carlo iterations during the ‘burn-in’ phase, and 10000 iterations during the final parameter determination step, assumed the default models for description of the continuum (DRWP, or ‘Cont\_Model’ in JAVELIN language) and line (‘RMap\_Model’) light curves, and solved for single continuum-line pairs at each time. Figure 6 presents the JAVELIN lag posterior distributions for the same sources presented in Figure 5.

Comparison between the histograms presented in Figure 5 and 6 shows that both methods roughly agree on the best determined lags. However, JAVELIN tends to present considerably compact probability distributions for most objects, in some cases with several well defined, extremely narrow peaks. As already observed by Fausnaugh et al. (2016), this is mostly because of the very strong – and seldom demonstrated – assumption that the emission line light curves are a simple lagged and smoothed version of the continuum emission. In fact, Fausnaugh et al. (2016) suggests that the actual dispersion is within  $2\sigma - 3\sigma$  of the JAVELIN quoted errors. In a few cases (e.g., CT1061), the JAVELIN results are very close to those found by our ICCF analysis.

JAVELIN results do not show spurious peaks at the edges of the probability distributions, which is also a consequence of the assumption of a BLR responding to the continuum light curves. Finally, it is interesting to notice some cases with contradicting results between the methods. For example, JAVELIN fails to determine a MgII lag for CT252, while the ICCF method detects a clear lag around 550 days which however, contains only 5% of the original CCCD distribution (this is in contrast with the CIV lag for CT975, with a 1% peak observed in the reliable region of the CCCD, which JAVELIN recovers successfully). At the same time, JAVELIN finds a well behaved peak at around 1000 days for the SiIV line in CT953, while the ICCF only finds a very shallow peak.

Since our main aim is to find statistically sound lags for

our sample of luminous quasars, for the analysis and discussion in the next sections we will use the more conservative ICCF and CCCD-based lags and error estimates as representative line lags for our sources.

## 5. RADIUS–LUMINOSITY RELATIONS

The radius–luminosity relation represents a milestone for the determination of the masses of black holes hosted by AGN. Here we will update the radius–luminosity relation for the CIV emission line first presented by Peterson et al. (2005, 2006) and later extended to higher luminosities by Kaspi et al. (2007) and Trevese et. (2014). To our knowledge, no determination of the radius–luminosity relations for the Ly $\alpha$  has previously been attempted, as no results for objects above  $\lambda L_\lambda(1350\text{\AA}) = 10^{45}$  ergs s $^{-1}$  had been reported until now.

In what follows we only construct radius–luminosity relations for objects where the lags are inconsistent with zero at a  $1\sigma$  level, this is, when  $\tau_{cent}/\sigma_- > 1$ . UV  $\lambda L_\lambda(1350\text{\AA})$  luminosities were obtained from the mean spectra of each quasar and are reported in Table 1. The errors represent the rms variation observed in the R-band continuum light curves. Scatter in the radius–luminosity correlations is given in each plot, where the first value corresponds to the observed scatter and the second value corresponds to the scatter due to measurement errors.

A linear regression was determined for each radius–luminosity relation using the bivariate method (BCES) of Akritas & Bershady (1996), which takes into account errors in both, the lags and the luminosities. As our lag error determinations are not symmetrical, we use the mean of both confidence limits as a first guess for the lag error of each data point and iterate so that the final error bar considered ( $\sigma_-$  or  $\sigma_+$ ) is determined by whether the points are found above or below the best fit solution. Convergence was always found after a few iterations.

### 5.1. The CIV Radius–Luminosity relation

For luminosities below  $\lambda L_\lambda(1350\text{\AA}) = 10^{45}$  ergs s $^{-1}$ , CIV lag measurements are compiled in Peterson et al. (2005, 2006) and Metzroth et al. (2006), and a very recent determination for NGC5548 is found in De Rosa et al. (2015). Two sources above this luminosity limit have been published: S5 0836+71 by Kaspi et al. (2007), and PG1247+267 by Trevese et al. (2014). Using the ICCF method it is not possible, however, to determine the lag for PG1247+267, as Trevese et al. (2014) also pointed out, and therefore we will not include this source in our CIV radius–luminosity determination. Our work adds to the list seven new high luminosity sources, namely, CT1061, CT286, CT564, CT650, CT953, J214355 and J221516.

In Figure 7 we present the results from the linear regression to the CIV radius–luminosity relation together with the lag and luminosity measurements. Following Kaspi et al. (2007), we write the CIV radius–luminosity in the following way:

$$\frac{R_{\text{CIV}}}{10 \text{ lt} - \text{days}} = (0.22 \pm 0.10) \left[ \frac{\lambda L_\lambda(1345\text{\AA})}{10^{43} \text{ erg s}^{-1}} \right]^{(0.46 \pm 0.08)} \quad (1)$$

The updated CIV radius–luminosity relation is very close to that reported by Kaspi et al. (2007), albeit

TABLE 4  
CROSS-CORRELATION ANALYSIS

	Ly $\alpha$				SiIV			
	$\tau_{cent}$ (days)	$\sigma_-$ (days)	$\sigma_+$ (days)	$M_{BH}$ ( $10^9 M_\odot$ )	$\tau_{cent}$ (days)	$\sigma_-$ (days)	$\sigma_+$ (days)	$M_{BH}$ ( $10^9 M_\odot$ )
CT1061	431 (99)	239 (55)	461 (106)	—	—	—	—	—
CT250	37 (11)	65 (19)	155 (45)	—	174 (51)	652 (191)	988 (290)	—
CT286	1191 (335)	78 (22)	542 (153)	$0.6 \pm 0.2$	427 (120)	205 (58)	395 (111)	$0.7 \pm 0.5$
CT320	-222 (-56)	105 (26)	365 (92)	—	1818 (459)	105 (26)	345 (87)	$3.9 \pm 0.6$
CT406	16 (5)	105 (29)	505 (141)	—	—	—	—	—
CT564	426 (102)	193 (46)	647 (155)	—	—	—	—	—
CT650	548 (150)	54 (15)	56 (15)	$0.16 \pm 0.02$	—	—	—	—
CT953	465 (127)	193 (53)	87 (24)	$1.8 \pm 0.6$	779 (213)	637 (174)	1153 (315)	—
CT975	—	—	—	—	—	—	—	—
HB89	1543 (438)	171 (48)	399 (113)	$1.4 \pm 0.3$	349 (99)	147 (42)	693 (196)	—
J214355	724 (187)	469 (121)	161 (42)	$1.3 \pm 0.6$	—	—	—	—
J221516	637 (185)	43 (13)	147 (43)	$0.22 \pm 0.04$	—	—	—	—
	CIV				CIII]			
	$\tau_{cent}$ (days)	$\sigma_-$ (days)	$\sigma_+$ (days)	$M_{BH}$ ( $10^9 M_\odot$ )	$\tau_{cent}$ (days)	$\sigma_-$ (days)	$\sigma_+$ (days)	$M_{BH}$ ( $10^9 M_\odot$ )
CT1061	397 (91)	105 (24)	485 (111)	—	—	—	—	—
CT250	-24 (-7)	184 (54)	356 (104)	—	—	—	—	—
CT286	1629 (459)	327 (92)	253 (71)	$1.1 \pm 0.2$	—	—	—	—
CT320	217 (55)	333 (84)	67 (17)	—	162 (41)	169 (43)	451 (114)	—
CT406	411 (115)	310 (86)	230 (64)	$0.7 \pm 0.5$	—	—	—	—
CT564	419 (100)	106 (25)	674 (161)	—	—	—	—	—
CT650*	592 (162)	38 (10)	122 (33)	$0.4 \pm 0.1$	—	—	—	—
CT953†	256 (70)	204 (56)	406 (111)	—	417 (114)	445 (122)	1355 (370)	—
CT975†	289 (77)	33 (9)	157 (42)	$0.5 \pm 0.2$	—	—	—	—
HB89	—	—	—	—	343 (97)	311 (88)	449 (127)	—
J214355	493 (128)	318 (82)	352 (91)	$0.9 \pm 0.6$	—	—	—	—
J221516	566 (165)	43 (13)	337 (98)	$0.3 \pm 0.1$	—	—	—	—
	MgII							
	$\tau_{cent}$ (days)	$\sigma_-$ (days)	$\sigma_+$ (days)	$M_{BH}$ ( $10^9 M_\odot$ )				
CT252†	550 (190)	170 (59)	330 (114)	—				

Lags are given in days in the observed frame and, in parenthesis, in the rest frame.

Black Hole virial masses are given assuming a virial factor of 1.

$M_{BH}$  values are presented only for objects where  $\tau_{cent}/\sigma_- > 1$  and  $\tau_{cent}/\sigma_+ > 1$ .

\* Centroid calculations for the CT650 CIV line failed in 60% of the trials.

† The MgII lag for CT252, CIII] for CT953, and CIV for CT975 are not considered reliable as they were obtained from less than 50% of the original CCD distributions.

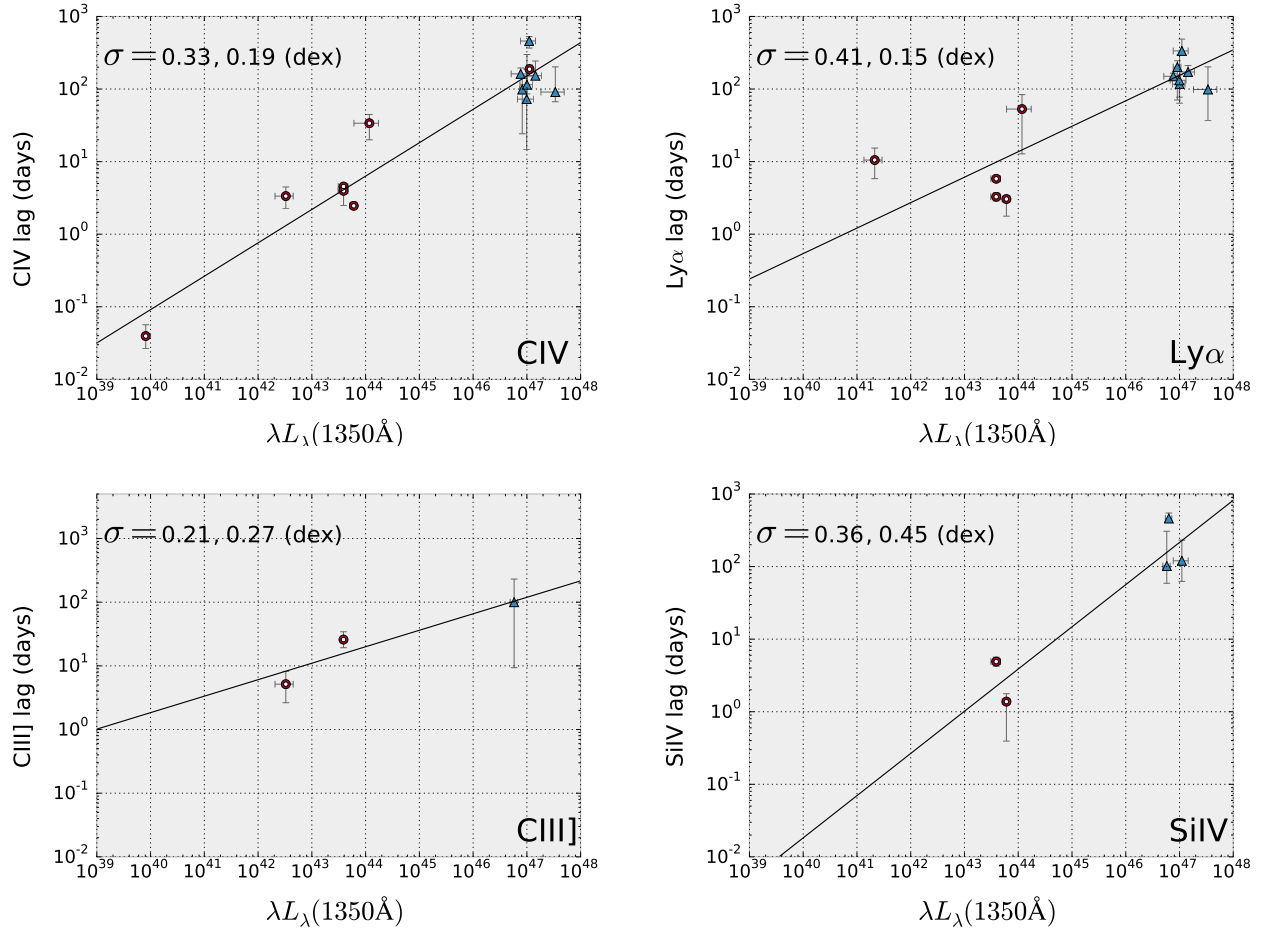


FIG. 7.— Radius–luminosity relations for the Ly $\alpha$ , CIV, CIII] and SiIV emission lines. Our sources are presented with blue solid triangles, while sources taken from the literature are presented with red circles. The solid black lines show the linear regression to the data using a bivariate analysis. Two values of  $\sigma$  are shown at the top left of each panel, where the first value corresponds to the observed scatter and the second value corresponds to the scatter due to measurement errors.

with slightly larger uncertainties. This is because we have included the mean from two lag measurements of NGC4151 taken from Metzroth et al. (2006), which helped to bridge the luminosity gap between the more luminous Seyfert galaxies and the dwarf Seyfert NGC4395 ( $\lambda L_{\lambda}(1350\text{\AA}) \sim 10^{40}$  ergs s $^{-1}$ ), but added more dispersion to the relation. Also, the two measurements for the NGC4395 lag have been averaged, reducing the weight of the measurements at the very low luminosity end.

We remind the reader that a well determined radius–luminosity relation for CIV does not solve the issues of using CIV as a well calibrated mass estimator for AGN, as the main problems with this line is the difficulty to determine a velocity that would reflect a virialized component of the velocity field of the line (see further discussion in Section 6.3 and e.g., Baskin & Laor 2005; Denney et al. 2012, 2016; Mejía-Restrepo et al. 2016, and references therein).

### 5.2. The Ly $\alpha$ Radius–Luminosity relation

From our sample, CT1061, CT286, CT564, CT650, CT953, J214355 and J221516 show significant lags and well determined uncertainties and will be considered for the determination of the Ly $\alpha$  radius–luminosity relation.

In order to have homogenous measurements, we re-determined the Ly $\alpha$  lags for the Seyfert galaxies monitored by the International AGN Watch<sup>6</sup> using the ICCF FR/RSS code that we employed with our sources. This is motivated by the improvements introduced to the FR/RSS code following Peterson et al. (2004), since all AGN Watch results were obtained previous to that date. We found significant lag constraints for NGC3783 (3.5 $^{+1.6}_{-2.0}$  days), NGC7469 (2.0 $^{+0.2}_{-1.3}$  days), Fairall 9 (9.4 $^{+5.1}_{-4.9}$  days), and 3C390.3 (61 $^{+33}_{-42}$  days) which were originally published by Reichert et al. (1994), Wanders et al. (1997), Rodriguez-Pascual et al. (1997) and O’Brien et al. (1998), respectively. Finally, we added the recent results for NGC5548 from De Rosa et al. (2015) which gives a lag of 5.9 $^{+0.3}_{-0.3}$  days during the ‘non-anomalous’ period of the campaign.

The analytical expressions found for the radius–luminosity relation using the linear regression is as follows:

$$\frac{R_{\text{Ly}\alpha}}{10 \text{ lt} - \text{days}} = (0.61 \pm 0.80) \left[ \frac{\lambda L_{\lambda}(1345\text{\AA})}{10^{43} \text{ erg s}^{-1}} \right]^{(0.35 \pm 0.19)} \quad (2)$$

Unfortunately, the Ly $\alpha$  radius–luminosity relation is not well constrained at the mid and low luminosity end, as the International AGN Watch sources show a very large dispersion and no very low-luminosity AGN has been monitored for this line.

### 5.3. The CIII] and SiIV Radius–Luminosity relations

A CIII] radius–luminosity relation was determined using lag measurements for NGC4151 (Metzroth et al. 2006) and a new analysis of the NGC5548 light curves originally presented by Clavel et al. (1991), which gave a lag of 26.3 $^{+8.3}_{-7.0}$  days. This work adds HB89 as the

only quasar from our sample that meets the requirement  $\tau_{\text{cent}}/\sigma_{-} > 1$ .

To determine a SiIV radius–luminosity relation, we re-analyzed the historical data for NGC7496 and 3C390.3 (Wanders et al. 1997 and O’Brien et al. 1998, respectively), but could only determine a significant lag of 1.4 $^{+0.4}_{-1.1}$  days for NGC7496. We add the recent determination for NGC5548 from De Rosa et al. (2015). CT286, CT320 and HB89 lag measurements from our sample are included. These relationships are presented in Figure 7. The resulting analytical expressions are as follows:

$$\frac{R_{\text{CIII]}}}{10 \text{ lt} - \text{days}} = (1.10 \pm 0.77) \left[ \frac{\lambda L_{\lambda}(1350\text{\AA})}{10^{43} \text{ erg s}^{-1}} \right]^{(0.26 \pm 0.16)} \quad (3)$$

$$\frac{R_{\text{SiIV}}}{10 \text{ lt} - \text{days}} = (0.10 \pm 0.10) \left[ \frac{\lambda L_{\lambda}(1350\text{\AA})}{10^{43} \text{ erg s}^{-1}} \right]^{(0.58 \pm 0.16)} \quad (4)$$

As with Ly $\alpha$ , the zero point of the SiIV radius–luminosity relation is very ambiguous because of the large dispersion observed in the Seyfert regime and the lack of any measurement for very low luminosity sources.

## 6. DISCUSSION

### 6.1. Sources with unexpected line variability

We have seen that 3/17 of our sources, i.e., 18 $^{+14}_{-9}\%$  assuming Poisson statistics (Gehrels 1986), show unexpected line variability, where the Ly $\alpha$  or SiIV emission line light curves do not seem to follow that of the observed UV continuum.

One possibility is that in these objects these emission lines never responds to the observed continuum. Another possibility, is that this is a transitional behavior due to changes in the BLR properties or the ionizing source.

Disengagement of the line response has not been generally reported among the Seyfert galaxies that have been subject to RM campaigns, although a non-linear response of CIV to the continuum variations was recognized in early observations of NGC5548 (see Maoz 1994). In fact, a clearer ‘anomalous’ behavior was seen in the very recent monitoring of NGC5548, where a departure of the line emission light curves is observed during  $\sim 1/3$  of the  $\sim 170$  day long campaign and where high ionization emission lines, in particular CIV, show a stronger disagreement with the continuum light curve than low ionization emission lines (Goad et al. 2016).

It seems that this behavior is more common in our sample of high luminosity quasars, even though the number of variability ‘events’ observed in the quasar light curves is usually smaller than those typically observed during seasonal monitoring campaigns of Seyfert galaxies. However, this result is based on limited data, while the different monitoring cadence, lengths of the campaigns and wide ranges in BH masses and accretion rates (which might ultimately drive the variability of the sources), complicate the comparison beyond the scope of this paper.

It is interesting to notice, however, that while in NGC5548 this behavior is strongest in the CIV line (with an ionization potential of 47.9 eV), in CT320, CT803 and

<sup>6</sup> <http://www.astronomy.ohio-state.edu/~agnwatch/>

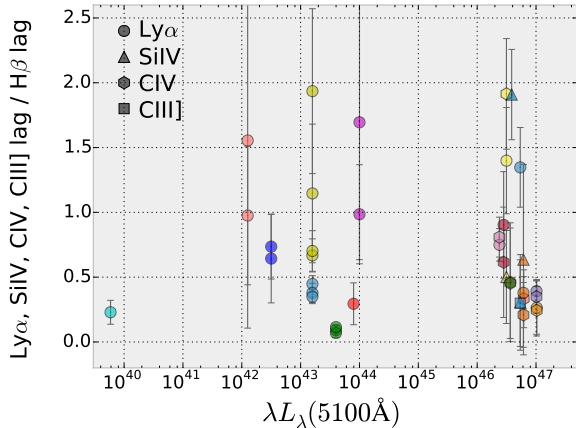


FIG. 8.— Ratio of  $\text{Ly}\alpha$ , SiIV, CIV and CIII] to  $\text{H}\beta$  lags. The  $\text{Ly}\alpha$ , SiIV, CIV and CIII] lags are those presented in Table 4 while the  $\text{H}\beta$  lags were predicted using the  $\lambda L_\lambda(5100\text{\AA})$  vs  $\text{H}\beta$  radius–luminosity correlation found in Bentz et al. (2013) and the inferred 5100Å luminosities (see text). Different shapes correspond to different emission lines (see legend), while different colors correspond to different sources. Seyfert galaxies are: NGC3783, NGC4151, NGC5548, NGC7469 and 3C390.3, as stated before. We have also added data from the 1989 campaign of NGC5548 and published by Clavel et al. (1991), as it includes the CIII] emission line (after re-calculating the lags using the ICCF FR/RSS code that we employed with our sources). The objects reported in this work are clustered at the high luminosity end of the diagram. Errors in the  $\text{Ly}\alpha$ , SiIV, CIV and CIII] lines were assumed as the average of the lower and upper  $1\sigma$  confidence limits in the lag measurements, while the scatter in the  $\text{H}\beta$  radius–luminosity correlation for the Clean2 sample from Bentz et al. (2013) was taken as the  $\text{H}\beta$  lag errors.

J224743 is SiIV and  $\text{Ly}\alpha$  that behave in an anomalous way. This might suggest that the cause is a different ionization continuum, as predicted for accretion disks around BHs of different masses but similar accretions rates (e.g., Davis & Laor, 2011), or seen in the relation between the  $\alpha_{ox}$  index (indicative of the fractional output in the X-ray and optical bands) with AGN luminosity (e.g., Vignali et al., 2003).

### 6.2. Location of the line emitting regions

One of the most significant and early results from RM in nearby Seyferts was the discovery that the BLR has a non-negligible radius and that different lines form at different distances from the central BH. From our cross correlation analysis we can revisit this result and try to extended it to a wider luminosity range.

Figure 8 presents the ratio of  $\text{Ly}\alpha$ , SiIV, CIII] and CIV lags to  $\text{H}\beta$  lags for Seyfert galaxies monitored by the International AGN Watch and quasars from this work deemed reliable in Table 4.  $\text{H}\beta$  lags were determined using the  $\lambda L_\lambda(5100\text{\AA})$  vs  $\text{H}\beta$  radius–luminosity correlation for the Clean2 sample in Bentz et al. (2013).  $\text{Ly}\alpha$ , SiIV, CIII] and CIV lags and associated confidence limits were taken from Table 4. Errors for these lines were assumed as the average of the lower and upper  $1\sigma$  limits. Errors in the  $\text{H}\beta$  lags were taken as the scatter reported for the radius–luminosity correlation determined by Bentz et al. (2013), i.e.,  $\sigma^2 = 0.018$ . 5100Å fluxes for our objects were obtained in the same way as in Section 2.1.2.

In general, we find a range of ratios that span up to a factor 6. However, most line lags are consistent with their emitting regions being interior to the predicted location

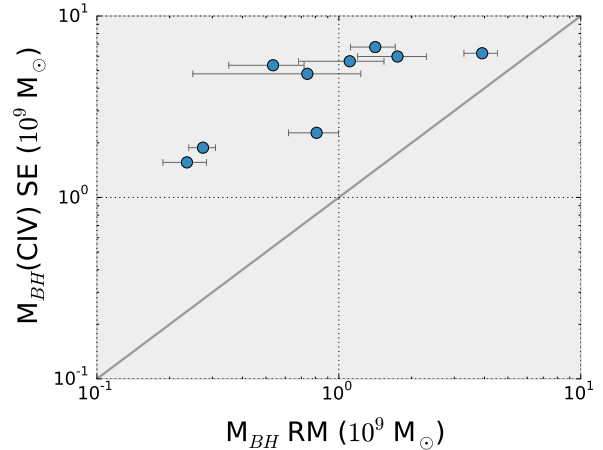


FIG. 9.— Comparison between Single–Epoch (SE) and Reverberation Mapping (RM) based BH masses, as presented in Tables 1 and 4. The thick gray line corresponds to the 1:1 relation.

of  $\text{H}\beta$ . There is also no clear stratification among the four lines for which we have determined lags in this work, suggesting that they are all produced at similar distances from the central black hole. There is no evidence for a clear dependency of the ratios with luminosity. This can be quantified comparing the lag cumulative distributions of Seyfert and quasars for *all* line ratios shown in Figure 8 using a KS test, which yields a p-value of 0.23, suggesting that the two distributions are very similar. This indicates that sources spanning 5 orders of magnitude in luminosity present a homologous BLR structure.

Notice the change in line ratios between the modern results for NGC5548 (in blue) taken from De Rosa et al. (2015), when compared with the historic values (in yellow) published by Clavel et al. (1991). This seems to be evidence of a restructuring of the BLR in this source, with the line emitting regions moving further in, despite a very small change in the UV and optical luminosities between these epochs. This also includes the  $\text{H}\beta$  location, as shown in Pei et al. (2017), with the lag about five times shorter than expected based on past measurements and the  $\text{H}\beta$  radius–luminosity correlation from Bentz et al. (2013).

Another interesting result is that all radius–luminosity relation slopes in Equations (1)–(5) are consistent at the  $2\sigma$  level with the naïvely expected value of 0.5, as predicted by the assumption of a photoionized BLR where the mean ionization parameter and mean density at the peak emissivity for a certain line remain constant (see Bentz et al. 2013 for further discussion). Notice, however, that some of the slopes, such as that of the CIII] line, have rather large errors.

### 6.3. Black hole masses from RM and SE methods

In Table 4 we give BH masses for sources with lags determined at a  $1\sigma$  level in the uncertainties at both sides of the probability CCD distribution, this is,  $\tau_{cent}/\sigma_- > 1$  and  $\tau_{cent}/\sigma_+ > 1$ . Masses were obtained as  $M_{\text{BH}}^{\text{RM}} = f \times \tau_{cent} \times c \times \text{FWHM}^2$ , where  $f$  is the virial factor,  $\tau_{cent}$  is the ICCF lag centroid reported in Table 4, and the FWHMs were measured from the mean spectra of each quasar and found in Table 2. Because of the noisy nature



of the emission lines in the rms spectra of our objects (see Figure 3), we only measured the FWHMs from the total mean flux spectra. We have adopted a virial factor  $f = 1$ , also assumed for the SE determinations. A good agreement is seen for RM masses obtained using different lines, with all results consistent within a  $2\sigma$  level.

Inspection of Tables 1 and 4 shows that RM masses ( $M_{\text{BH}}^{\text{RM}}$ ) are systematically smaller than those obtained using the CIV single-epoch (SE) method ( $M_{\text{BH}}^{\text{SE}}$ ), which were determined using  $M_{\text{BH}}^{\text{SE}} = 10^{6.353} \times (L_{1450})^{0.599} \times \text{FWHM}^2$  as presented in Mejía-Restrepo et al. (2016). Again, the FWHM values are those presented in Table 1. The results can be seen in Figure 9, where the mean of the RM masses is plotted when lags from more than one line are available for a single object. Our results suggest that, on average,  $M_{\text{BH}}^{\text{SE}}$  are overestimated when compared with  $M_{\text{BH}}^{\text{RM}}$ . The discrepancy is probably driven by the non-virial behavior of the CIV line width. The SE cross-calibration of CIV assumes that the region responsible for the emission of this line obeys  $R_{\text{H}\beta}/R_{\text{CIV}} = (\text{FWHM}(\text{H}\beta)/\text{FWHM}(\text{CIV}))^{-2}$  (since SE masses obtained from H $\beta$  and CIV must satisfy  $M_{\text{BH}}^{\text{SE}}(\text{H}\beta) = M_{\text{BH}}^{\text{SE}}(\text{CIV})$ ). As we just determined for our quasars,  $R_{\text{CIV}}/R_{\text{H}\beta} \sim 0.5$  and we would expect that  $(\text{FWHM}(\text{H}\beta)/\text{FWHM}(\text{CIV}))^2 \sim 0.5$  or  $\text{FWHM}(\text{CIV}) \sim 1.4 \times \text{FWHM}(\text{H}\beta)$  for a virialized system. However, typically it is found that CIV is narrower than this, suggesting a dominant non-virialized component in many sources (see Trakhtenbrot & Netzer, 2012).

## 7. SUMMARY

For the first time we have presented RM results for a substantial number of luminous quasars found at  $z \gtrsim 2$ . From our results we can summarize the following:

- Out of 17 quasars with spectroscopic follow up 14 show that all their emission line light curves seem to reverberate in response to the variations observed in the continuum light curves, while 3/17 show peculiar behavior in one emission line. This might suggest that the observed R-band continuum in these three sources does not follow the

changes that the ionizing continuum experiences.

- Reliable lag measurements are determined for 11 quasars for the Ly $\alpha$  emission line, 5 quasars for the SiIV emission line, 11 for the CIV emission line, and 2 quasars for the CIII] emission line (Table 4). However, only  $\sim 1/2$  of the determined lags have  $\tau_{\text{cent}}/\sigma > 1$  and are therefore sufficiently constrained to allow for the determination of BH masses.
- Radius–luminosity relations for Ly $\alpha$ , SiIV, CIV, and CIII] are presented using our data and previous lag determinations. Slopes are well constrained for all correlations and are found to be less than  $2\sigma$  away from the predicted value of 0.5, although the Ly $\alpha$  and CIII] relations present large fractional errors.
- We find that the regions responsible for the emission of Ly $\alpha$ , SiIV, CIV, CIII] are commonly interior to that producing H $\beta$ . At the same time, there is no clear stratification among them. This is found to be the case across 5 orders of magnitude in continuum luminosity.
- For those quasars with lags determined at a  $1\sigma$  level (for both,  $\sigma_-$  and  $\sigma_+$ ), we determined BH masses using the observed emission line FWHMs. The RM masses are systematically smaller than those determined from single-epoch CIV calibrations. This is consistent with a significant non-virialized component to the CIV line profile.

This project would have never been possible without the support of the Chilean National TAC (CNTAC) which during more than 10 years allocated hundreds of nights of telescope time to conduct our reverberation campaign. We also thank Brad Peterson and Mario Hamuy for facilitating code used in the analysis of the data. Finally, we also thank the anonymous referee for the suggestion to use MC to determine line light curve errors. PL acknowledges support by Fondecyt along all these years, and in particular to Project #1161184.

## REFERENCES

- Alexander, T. 1997, *Astronomical Time Series*, 218, 163  
 Baskin, A., & Laor, A. 2005, *MNRAS*, 356, 1029  
 Bentz, M. C., Peterson, B. M., Netzer, H., Pogge, R. W., & Vestergaard, M. 2009, *ApJ*, 697, 160  
 Bentz, M. C., Denney, K. D., Grier, C. J., et al. 2013, *ApJ*, 767, 149  
 Bentz, M. C., Peterson, B. M., Pogge, R. W., Vestergaard, M., & Onken, C. A. 2006, *ApJ*, 644, 133  
 Blandford, R. D., & McKee, C. F. 1982, *ApJ*, 255, 419  
 Bongiorno, A., Zamorani, G., Gavignaud, I., et al. 2007, *A&A*, 472, 443  
 Cardelli, J. A., Clayton, G. C., & Mathis, J. S. 1989, *ApJ*, 345, 245  
 Chhetri, R., Ekers, R. D., Jones, P. A., & Ricci, R. 2013, *MNRAS*, 434, 956  
 Cirasuolo, M., Magliocchetti, M., Celotti, A., & Danese, L. 2003, *MNRAS*, 341, 993  
 Condon, J. J., Cotton, W. D., Greisen, E. W., et al. 1998, *AJ*, 115, 1693  
 Collin, S., Kawaguchi, T., Peterson, B. M., & Vestergaard, M. 2006, *A&A*, 456, 75  
 Croom, S. M., Smith, R. J., Boyle, B. J., et al. 2004, *MNRAS*, 349, 1397  
 Cutri, R. M., Skrutskie, M. F., van Dyk, S., et al. 2003, *VizieR Online Data Catalog*, 2246  
 Davis, S. W., & Laor, A. 2011, *ApJ*, 728, 98  
 De Rosa, G., Peterson, B. M., Ely, J., et al. 2015, *ApJ*, 806, 128  
 Denney, K. D. 2012, *ApJ*, 759, 44  
 Denney, K. D., Horne, K., Shen, Y., et al. 2016, *ApJS*, 224, 14  
 Edelson, R., Gelbord, J. M., Horne, K., et al. 2015, *ApJ*, 806, 129  
 Edelson, R. A., & Krolik, J. H. 1988, *ApJ*, 333, 646  
 Fausnaugh, M. M., Denney, K. D., Barth, A. J., et al. 2016, *ApJ*, 821, 56  
 Fausnaugh, M. M., Starkey, D. A., Horne, K., et al. 2018, *ApJ*, 854, 107  
 Gehrels, N. 1986, *ApJ*, 303, 336  
 Goad, M. R., Korista, K. T., De Rosa, G., et al. 2016, *ApJ*, 824, 11  
 Kormendy, J., & Ho, L. C. 2013, *ARA&A*, 51, 511

- Hewitt, A., & Burbidge, G. 1989, *ApJS*, 69, 1
- Kasliwal, V. P., Vogeley, M. S., & Richards, G. T. 2015, *MNRAS*, 451, 4328
- Kaspi, S., Brandt, W. N., Maoz, D., et al. 2007, *ApJ*, 659, 997
- Kaspi, S., Smith, P. S., Netzer, H., et al. 2000, *ApJ*, 533, 631
- Kaspi, S., Maoz, D., Netzer, H., et al. 2005, *ApJ*, 629, 61
- Kelly, B. C., Bechtold, J., & Siemiginowska, A. 2009, *ApJ*, 698, 895
- Korista, K. T., Alloin, D., Barr, P., et al. 1995, *ApJS*, 97, 285
- Lal, D. V., & Ho, L. C. 2010, *AJ*, 139, 1089
- Lira, P., Arévalo, P., Uttley, P., McHardy, I. M. M., & Videla, L. 2015, *MNRAS*, 454, 368
- Maoz, D., Netzer, H., Leibowitz, E., et al. 1990, *ApJ*, 351, 75
- Maoz, D. 1994, *Reverberation Mapping of the Broad-Line Region in Active Galactic Nuclei*, 69, 95
- Mauch, T., Murphy, T., Buttery, H. J., et al. 2003, *MNRAS*, 342, 1117
- Mejía-Restrepo, J. E., Trakhtenbrot, B., Lira, P., Netzer, H., & Capellupo, D. M. 2016, *MNRAS*, 460, 187
- Metzroth, K. G., Onken, C. A., & Peterson, B. M. 2006, *ApJ*, 647, 901
- Momjian, E., Carilli, C. L., Walter, F., & Venemans, B. 2014, *AJ*, 147, 6
- Mudd, D., Martini, P., Zu, Y., et al. 2017, *arXiv:1711.11588*
- Onken, C. A., & Peterson, B. M. 2002, *ApJ*, 572, 746
- O'Brien, P. T., Dietrich, M., Leighly, K., et al. 1998, *ApJ*, 509, 163
- Pei, L., Fausnaugh, M. M., Barth, A. J., et al. 2017, *ApJ*, 837, 131
- Peterson, B. M., Wanders, I., Horne, K., et al. 1998, *PASP*, 110, 660
- Peterson, B. M., Ferrarese, L., Gilbert, K. M., et al. 2004, *ApJ*, 613, 682
- Peterson, B. M., Bentz, M. C., Desroches, L.-B., et al. 2005, *ApJ*, 632, 799
- Peterson, B. M., Bentz, M. C., Desroches, L.-B., et al. 2006, *ApJ*, 641, 638
- Peterson, B. M., Wanders, I., Horne, K., et al. 1998, *PASP*, 110, 660
- Reichert, G. A., Rodríguez-Pascual, P. M., Alloin, D., et al. 1994, *ApJ*, 425, 582
- Rodríguez-Pascual, P. M., Alloin, D., Clavel, J., et al. 1997, *ApJS*, 110, 9
- Ross, N. P., McGreer, I. D., White, M., et al. 2013, *ApJ*, 773, 14
- Saturni, F. G., Trevese, D., Vagnetti, F., Perna, M., & Dadina, M. 2016, *A&A*, 587, A43
- Shemmer, O., Netzer, H., Maiolino, R., et al. 2004, *ApJ*, 614, 547
- Trakhtenbrot, B., & Netzer, H. 2012, *MNRAS*, 427, 3081
- Trevese, D., Stirpe, G., Vagnetti, F., Zitelli, V., & Paris, D. 2006, *Astronomical Society of the Pacific Conference Series*, 360, 201
- Trevese, D., Perna, M., Vagnetti, F., Saturni, F. G., & Dadina, M. 2014, *ApJ*, 795, 164
- Ulrich, M.-H., Courvoisier, T. J.-L., & Wamsteker, W. 1993, *ApJ*, 411, 125
- Vanden Berk, D. E., Richards, G. T., Bauer, A., et al. 2001, *AJ*, 122, 549
- Vignali, C., Brandt, W. N., & Schneider, D. P. 2003, *AJ*, 125, 433
- Wanders, I., Peterson, B. M., Alloin, D., et al. 1997, *ApJS*, 113, 69
- Wang, R., Carilli, C. L., Beelen, A., et al. 2007, *AJ*, 134, 617
- Welsh, W., Robinson, E. L., Hill, G., et al. 2000, *Bulletin of the American Astronomical Society*, 32, 39.13
- Woo, J.-H., Yoon, Y., Park, S., Park, D., & Kim, S. C. 2015, *ApJ*, 801, 38
- Zu, Y., Kochanek, C. S., Kozłowski, S., & Udalski, A. 2013, *ApJ*, 765, 106
- Zu, Y., Kochanek, C. S., & Peterson, B. M. 2011, *ApJ*, 735, 80

## APPENDIX

Here we present the emission line and R-band continuum light curves for the quasar CT1061. The remaining light curves can be downloaded from the electronic journal database. In all tables dates are expressed in JD–2450000 days, and fluxes in units of  $10^{-14}$  ergs  $s^{-1}$   $cm^{-2}$  for the line measurements and  $10^{-16}$  ergs  $s^{-1}$   $cm^{-2}$   $\text{Å}^{-1}$  for the R-band light curves.

TABLE 5  
EMISSION LINE AND R-BAND CONTINUUM LIGHT CURVES FOR CT1061

Ly $\alpha$			SiIV			CIV			CIII]			R		
JD	flux	error	JD	flux	error	JD	flux	error	JD	flux	error	JD	flux	error
5270.8	27.19	0.44	5270.8	2.06	0.26	5270.8	8.12	0.12	5270.8	4.15	0.35	3403.9	5.50	0.08
5280.7	27.39	0.53	5280.7	1.90	0.32	5280.7	8.19	0.16	5280.7	3.96	0.31	3444.8	5.48	0.08
5658.6	27.04	0.46	5658.6	2.06	0.24	5658.6	8.01	0.13	5658.6	3.99	0.24	3490.7	5.55	0.08
5917.8	27.28	0.53	5917.8	2.04	0.26	5917.8	8.03	0.17	5917.8	4.20	0.29	3781.7	5.70	0.08
5945.8	27.26	0.50	5945.8	2.12	0.22	5945.8	8.12	0.14	5945.8	4.00	0.28	3846.7	5.52	0.08
6015.7	26.72	0.54	6015.7	1.92	0.26	6015.7	7.86	0.19	6015.7	3.73	0.30	3894.5	5.58	0.08
6017.7	27.42	0.50	6017.7	2.10	0.29	6017.7	8.10	0.17	6017.7	3.73	0.44	4140.9	5.48	0.08
6048.6	26.95	0.45	6048.6	1.95	0.29	6048.6	7.96	0.13	6048.6	4.36	0.33	4154.8	5.53	0.08
6298.8	26.83	0.37	6298.8	2.00	0.22	6298.8	8.04	0.12	6298.8	4.00	0.26	4168.9	5.58	0.08
6723.8	26.65	0.36	6723.8	1.90	0.20	6723.8	7.84	0.08	6723.8	4.46	0.31	4258.6	5.63	0.08
6783.6	26.68	0.53	6783.6	1.92	0.24	6783.6	8.00	0.21	6783.6	4.12	0.30	4272.5	5.69	0.08
7020.8	26.20	0.40	7020.8	1.90	0.24	7020.8	7.46	0.25	7020.8	3.77	0.34	4505.8	6.21	0.09
7759.0	26.30	0.47	7759.0	1.96	0.27	7759.0	7.75	0.11	7759.0	3.75	0.24	4579.7	6.36	0.09
—	—	—	—	—	—	—	—	—	—	—	—	4580.5	6.22	0.09
—	—	—	—	—	—	—	—	—	—	—	—	4856.7	6.58	0.09
—	—	—	—	—	—	—	—	—	—	—	—	4889.8	6.71	0.09
—	—	—	—	—	—	—	—	—	—	—	—	4910.8	6.63	0.09
—	—	—	—	—	—	—	—	—	—	—	—	4944.7	6.76	0.09
—	—	—	—	—	—	—	—	—	—	—	—	5010.5	6.78	0.09
—	—	—	—	—	—	—	—	—	—	—	—	5235.8	6.48	0.09
—	—	—	—	—	—	—	—	—	—	—	—	5264.7	6.50	0.09
—	—	—	—	—	—	—	—	—	—	—	—	5270.8	6.70	0.04
—	—	—	—	—	—	—	—	—	—	—	—	5274.7	6.60	0.09
—	—	—	—	—	—	—	—	—	—	—	—	5280.7	6.65	0.04
—	—	—	—	—	—	—	—	—	—	—	—	5306.7	6.55	0.09
—	—	—	—	—	—	—	—	—	—	—	—	5628.8	6.16	0.08
—	—	—	—	—	—	—	—	—	—	—	—	5628.8	6.20	0.09
—	—	—	—	—	—	—	—	—	—	—	—	5653.8	6.21	0.09
—	—	—	—	—	—	—	—	—	—	—	—	5653.8	6.25	0.09
—	—	—	—	—	—	—	—	—	—	—	—	5658.6	6.21	0.04
—	—	—	—	—	—	—	—	—	—	—	—	5666.7	6.32	0.09
—	—	—	—	—	—	—	—	—	—	—	—	5666.7	6.25	0.09
—	—	—	—	—	—	—	—	—	—	—	—	5738.5	6.12	0.08
—	—	—	—	—	—	—	—	—	—	—	—	5738.5	6.13	0.08
—	—	—	—	—	—	—	—	—	—	—	—	5917.8	6.01	0.04
—	—	—	—	—	—	—	—	—	—	—	—	5929.7	6.01	0.08
—	—	—	—	—	—	—	—	—	—	—	—	5929.7	5.96	0.08
—	—	—	—	—	—	—	—	—	—	—	—	5945.8	5.95	0.04
—	—	—	—	—	—	—	—	—	—	—	—	6013.6	5.79	0.08
—	—	—	—	—	—	—	—	—	—	—	—	6013.6	5.76	0.08
—	—	—	—	—	—	—	—	—	—	—	—	6015.7	5.54	0.04
—	—	—	—	—	—	—	—	—	—	—	—	6017.7	5.86	0.04
—	—	—	—	—	—	—	—	—	—	—	—	6033.6	5.79	0.08
—	—	—	—	—	—	—	—	—	—	—	—	6033.6	5.75	0.08
—	—	—	—	—	—	—	—	—	—	—	—	6048.6	5.85	0.04
—	—	—	—	—	—	—	—	—	—	—	—	6049.5	5.72	0.08
—	—	—	—	—	—	—	—	—	—	—	—	6049.5	5.70	0.08
—	—	—	—	—	—	—	—	—	—	—	—	6298.7	5.53	0.08
—	—	—	—	—	—	—	—	—	—	—	—	6298.7	5.44	0.08
—	—	—	—	—	—	—	—	—	—	—	—	6298.8	5.54	0.04
—	—	—	—	—	—	—	—	—	—	—	—	6303.7	5.54	0.08
—	—	—	—	—	—	—	—	—	—	—	—	6303.8	5.63	0.11
—	—	—	—	—	—	—	—	—	—	—	—	6306.7	5.60	0.08
—	—	—	—	—	—	—	—	—	—	—	—	6306.7	5.50	0.08
—	—	—	—	—	—	—	—	—	—	—	—	6400.6	5.33	0.07
—	—	—	—	—	—	—	—	—	—	—	—	6723.8	5.19	0.04
—	—	—	—	—	—	—	—	—	—	—	—	6783.6	5.14	0.04
—	—	—	—	—	—	—	—	—	—	—	—	7020.8	5.26	0.04
—	—	—	—	—	—	—	—	—	—	—	—	7109.6	5.28	0.07
—	—	—	—	—	—	—	—	—	—	—	—	7123.6	5.24	0.07
—	—	—	—	—	—	—	—	—	—	—	—	7152.5	5.40	0.07
—	—	—	—	—	—	—	—	—	—	—	—	7181.5	5.37	0.07
—	—	—	—	—	—	—	—	—	—	—	—	7182.4	5.38	0.07
—	—	—	—	—	—	—	—	—	—	—	—	7225.5	5.35	0.29
—	—	—	—	—	—	—	—	—	—	—	—	7759.0	5.34	0.04